UNIVERSIDADE DE SÃO PAULO
ESCOLA DE ENGENHARIA DE SÃO CARLOS

LORENA DARIANE DA SILVA ALENCAR

Characterization of $BaMoO_4$, $BaWO_4$, $CaWO_4$ and $CaMoO_4$ compounds obtained by polymeric precursor method and by microwave-assisted hydrothermal method.

Caracterização dos compostos $BaMoO_4$, $BaWO_4$, $CaWO_4$ e $CaMoO_4$ obtidos pelos métodos dos precursores poliméricos e hidrotermal assistido por micro-ondas

São Carlos

2018

LORENA DARIANE DA SILVA ALENCAR

Characterization of $BaMoO_4$, $BaWO_4$, $CaWO_4$ and $CaMoO_4$ compounds obtained by polymeric precursor method and by microwave-assisted hydrothermal method

Caracterização dos compostos $BaMoO_4$, $BaWO_4$, $CaWO_4$ e $CaMoO_4$ obtidos pelos métodos dos precursores poliméricos e hidrotermal assistido por micro-ondas

Corrected Version

(Original version available on the Program Unit)

Thesis presented to the Graduate Program in Materials Science and Engineering at Universidade de São Paulo to obtain the degree of Doctor of Science.

Concentration area: Development, Characterization and Application of Materials

Supervisor: Dr. Maria Inês Basso Bernardi

São Carlos

2018

Ficha catalográfica elaborada pela Biblioteca Prof. Dr. Sérgio Rodrigues Fontes da EESC/USP com os dados inseridos pelo(a) autor(a).

A368c

Alencar, Lorena Dariane da Silva
Characterization of BaMoO4, BaWO4, CaWO4 and CaMoO4 compounds obtained by polymeric precursor method and by microwave-assisted hydrothermal method - Caracterização dos compostos BaMoO4, BaWO4, CaWO4 e CaMoO4 obtidos pelos métodos dos precursores poliméricos e hidrotermal assistido por micro-ondas / Lorena Dariane da Silva Alencar; orientadora Maria Inês Basso Bernardi. São Carlos, 2018.

Tese (Doutorado) - Programa de Pós-Graduação em Ciência e Engenharia de Materiais e Área de Concentração em Desenvolvimento, Caracterização e Aplicação de Materiais -- Escola de Engenharia de São Carlos da Universidade de São Paulo, 2018.

1. Molybdate. 2. Tungstate. 3. Toluene. 4. XANES. 5. EXAFS. I. Título.

FOLHA DE JULGAMENTO

Candidata: Licenciada **LORENA DARIANE DA SILVA ALENCAR.**

Título da tese: "Caracterização dos compostos $BaMoO_4$, $BaWO_4$, $CaWO_4$ e $CaMoO_4$ obtidos pelos métodos dos precursores poliméricos e hidrotermal assistido por micro-ondas".

Data da defesa: 15/05/2018.

Comissão Julgadora: **Resultado:**

Dra. **Maria Ines Basso Bernardi** APROVADA
(Presidente)
(Instituto de Física de São Carlos/IFSC)

Prof. Associado **Rafael Salomão** APROVADA
(Escola de Engenharia de São Carlos/EESC)

Prof. Dr. **Alexandre Mesquita** Aprovada
(Universidade Estadual Paulista "Júlio de Mesquita Filho"/UNESP – Rio Claro)

Profa. Dra. **Lilian Menezes de Jesus** APROVADA
(Universidade Federal de São Carlos/UFSCar)

Prof. Dr. **Fabio Simões de Vicente** APROVADA
(Universidade Estadual Paulista "Júlio de Mesquita Filho"/UNESP – Rio Claro)

- Coordenador do Programa de Pós-Graduação em Ciências e Engenharia de Materiais:
Prof. Titular **Antonio José Felix de Carvalho**

Presidente da Comissão de Pós-Graduação:
Prof. Associado **Luís Fernando Costa Alberto**

To my parents,

José A. Alencar e Ivanira da Silva.

Acknowledgments

I would like to thank Dr. Maria Inês B. Bernardi, my supervisor, for her support, friendship and teaching during my PhD.

Prof. Dr. Alexandre Mesquita (UNESP/ Rio Claro) for X-ray absortion measurements, the scientific discussions and help throughout this thesis.

Prof. Dr. Maximo Siu Li (IFSC/USP), I thank him for the help in samples preparation and photoluminescence measurements.

Prof. Dr. Humberto Fajardo (UFOP) for the catalysis measurements and discussion of the results.

Prof. Dr. Jacques Noudem and Dr. Ulrike Lüders (CRISMAT-UNICAEN/France) for receiving me in their laboratory and help with samples preparation.

The technicians of our group (CCMC/IFSC) Cássio Domenicucci, Geraldo Frigo, Wagner Correr, Luiz Carashi, Manoel Roncon and Erica Signini.

My friends and colleagues from CCMC/USP for the friendship and the scientific discussions.

I thank Universidade de São Paulo and the PGr-CEM.

I thank National Laboratory of Synchroton Light (LNLS) for the infrastructure.

To CAPES (BEX-6669/15-8), FAPESP and CNPq for the financial support .

ABSTRACT

ALENCAR, L.D.S. **Characterization of $BaMoO_4$, $BaWO_4$, $CaWO_4$ and $CaMoO_4$ compounds obtained by polymeric precursor method and by microwave-assisted hydrothermal method**. Thesis (Doctor in Science) - Escola de Engenharia de São Carlos, Universidade de São Paulo, São Carlos, 2018.

Molybdates and tungstates belonging to the scheelite family constitute an important class of materials, which have advantages as a relatively low cost and being non-polluting. Barium molybdate ($BaMoO_4$), barium tungstate ($BaWO_4$), calcium molybdate ($CaMoO_4$) and calcium tungstate ($CaWO_4$) have been extensively studied due their photoluminescent properties, besides that they also present catalysis and photocatalysis applications. However, to the best of our knowledge there are no structural characterizations of $BaMoO_4$, $BaWO_4$ and $CaMoO_4$ by x-ray absorption spectroscopy (XAS) in the literature. In this work, powders of these 4 compounds were prepared by microwave-assisted hydrothermal (MAH) method and polymeric precursor method (PPM) and their structural properties were characterized by X-ray diffraction (XRD), X-ray absorption near edge spectroscopy (XANES) and extended X-ray absorption fine structure (EXAFS) measurements. The morphology and particle size of these crystalline powders were observed by field emission scanning electron microscopy (FE-SEM). Furthermore, $BaMoO_4$, $BaWO_4$ and $CaWO_4$ were employed as solid catalysts towards gas phase toluene oxidation reactions and their optical properties were investigated by ultraviolet visible (UV-Vis) absorption and photoluminescence (PL) measurements. XRD patterns confirm the phase purity of materials from both preparation methods and reveal a preferential growth when the powders are prepared by MAH due polymeric agents and processing using microwave, which was confirmed by FE-SEM. XANES and EXAFS results show that the preparation method did not introduce high disorders into the structure, however the H_2 Temperature-Programmed Reduction (H_2-TPR) measurements indicated that the

catalyst reducibility is affected by the preparation method of the samples. PL emissions were attributed to the charge-transfer transitions within the $[WO_4]^{2-}$ and $[MoO_4]^{2-}$ complexes.

Keywords: Molybdate. Tungstate. Toluene. XANES. EXAFS.

RESUMO

ALENCAR, L.D.S. **Caracterização dos compostos $BaMoO_4$, $BaWO_4$, $CaWO_4$ e $CaMoO_4$ obtidos pelos métodos dos precursores poliméricos e hidrotermal assistido por micro-ondas**. Tese (Doutorado em Ciências) - Escola de Engenharia de São Carlos, Universidade de São Paulo, São Carlos, 2018.

Os óxidos molibdatos e tungstatos, pertencentes à família das scheelitas, constituem uma importante classe de materiais que apresentam a vantagem de possuírem relativo baixo custo e não serem poluentes. Molibdato de bário ($BaMoO_4$), tungstato de bário ($BaWO_4$), molibdato de cálcio ($CaMoO_4$) e o tungstato de cálcio ($CaWO_4$) têm sido extensivamente estudados devido às suas propriedades fotoluminescentes, além de apresentarem aplicações em catálise e fotocatálise. No entanto, não foi encontrada na literatura caracterizações estruturais de $BaMoO_4$, $BaWO_4$ e $CaMoO_4$ por espectroscopia de absorção de raios X (XAS). Neste trabalho, partículas destes quatro compostos foram preparados pelo método hidrotermal assistido por micro-ondas (MAH) e método dos precursores poliméricos (PPM). Suas propriedades estruturais foram caracterizadas por difração de raios X (XRD) e espectroscopia de absorção de raios X na região XANES (do inglês *X-Ray Absorption Near Edge Structure*) e região EXAFS (do inglês *Extended X-Ray Absorption Fine Structure*). A morfologia e o tamanho de partícula desses pós cristalinos foram observados por microscopia eletrônica de varredura por emissão de campo (FE-SEM). Além disso, $BaMoO_4$, $BaWO_4$ e $CaWO_4$ foram empregados como catalisadores sólidos para as reações de oxidação de tolueno em fase gasosa e as suas propriedades ópticas foram investigadas por medidas de absorção no ultravioleta/visível (UV-Vis) e fotoluminescência (PL). Os padrões XRD confirmam a pureza de fase dos materiais obtidos em ambos os métodos de preparação e revelam um crescimento preferencial dos pós preparados por MAH devido aos agentes poliméricos e ao processamento usando micro-ondas, esse crescimento foi confirmado pelas micrografias obtidas por FE-SEM.

Os resultados de XANES e EXAFS mostram que o método de preparação não introduz desordens elevadas na estrutura, no entanto, as medidas de redução à temperatura programada (H_2-TPR) indicaram que a redução do catalisador é afetada pelo método de preparação das amostras. As emissões de PL foram atribuídas às transições de transferência de carga dentro dos complexos $[WO_4]^{2-}$ e $[MoO_4]^{2-}$.

Palavras-chave: Molibdato. Tungstato. Tolueno. XANES. EXAFS.

LIST OF FIGURES

LIST OF TABLES

CONTENTS

1 INTRODUCTION

The molybdates and tungstates oxides constitute an important class of optoelectronics industrial materials due their optical properties.[1,2] These two mineral families have several promising applications such as electro optical devices,[3] solid-state lasers,[4] scintillators,[5] microwave dielectric ceramics,[6] fluorescent lamps,[7] negative electrodes for Li-ion battery[8] and cryogenic scintillators for the detection of Isotope ^{100}Mo.[9]

Tungstates with formula AWO_4 (A= Ca^{2+}, Sr^{2+}, Ba^{2+}) are of great scientific and technological interest because they have relatively low cost and are non-polluting, including them in the list of sustainable products.[10] Compared to the oxides formed by tungsten, those formed by molybdenum $AMoO_4$ have been less studied, but some molybdenum oxides with different morphologies were synthesized such as wires,[11] fibers,[12] dendrites,[13] nanobelt[14] and pompons.[15] These materials have the property of emitting blue or green light when activated by UV or X-ray radiation.[16] This property comes from distortions on the $[WO_4]$ and $[MoO_4]$ tetrahedral that form the structure.[17,18]

Considering the high scientific and technological interest in the study of tungstates and molybdates, the structural, optical and catalytic properties of the $BaMoO_4$, $BaWO_4$, $CaWO_4$ and $CaMoO_4$ powders were investigated in this work.

1.1 Molybdate and Tungstate

Molybdates and tungstates belonging to the scheelite family are characterized by space group $I4_1/a$ (n° 88), point group C_{4h} (4/m) and tetragonal-dipiramidal centrosymmetric crystalline system. They have molecular formula ABO_4 where the cations A have coordination number eight in a pseudo cubic approximation and the cations B have coordination number four in a tetrahedral approach in relation to the oxygen.[16]

Figure 1.1 shows the schematic representations of tetragonal ABO_4 unit cell. This structure was modeled through the Diamond program (version 2.1)[19] using $CaWO_4$ crystallographic data.

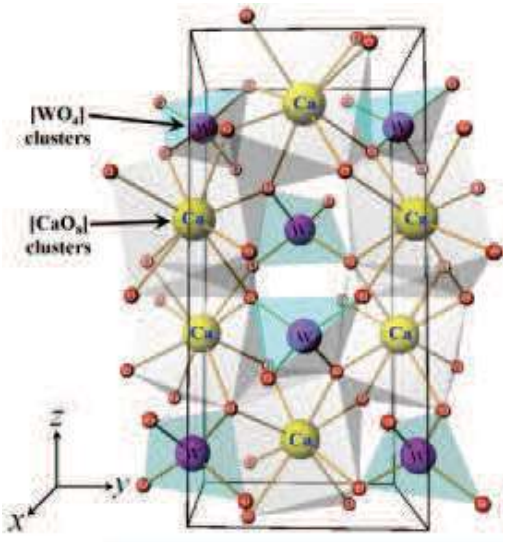

Figure 1.1. Schematic representation of tetragonal ABO_4 unit cell.

Source: Cavalcante et al.[16]

Various methods of synthesis have been used in the preparation of these compounds,[17,18,20,21] among these methods microwave-assisted hydrothermal (MAH) method and polymeric precursor method (PPM) were chosen for their synthesis in the present study.

1.2 Microwave-assisted hydrothermal (MAH)

The MAH is a technique of synthesis of low temperatures and short processing times with high heating rates when compared to other synthesis methods as the conventional hydrothermal, polymeric precursor method or mixtures of oxides.[16] In the conventional hydrothermal (hydro = water, thermal = heat)process, colloidal suspensions are prepared and aged in a stainless steel autoclave, with a polytetrafluoroethylene (PTFE) container inside it where the suspension is placed.The system is then sealed and heated. The pressure increase due to evaporation of the solvent until equilibrium is reached. Therefore, it will not occur to

the total evaporation of the liquid. The heating of the autoclave will supply energy to the system for the formation of the compounds and the growth of the particles.[22] However, conventional hydrothermal presents low yield and low crystallization speed when the reactions occur at moderate temperatures.

To increase the kinetics of crystallization, microwave radiation is combined with the hydrothermal process (MAH). The microwave radiation acts directly on the permanent dipoles of the solvent, which oscillate and transfer energy to the solute. The direct interaction of radiation with matter makes this process more efficient.[23]

1.3 Polymeric precursor method (PPM)

Polymeric precursor method is an effective soft chemical method to obtain multi-component oxides. This process promotes morphological and compositional homogeneities at the prepared complex oxide material, reducing segregation of the metals, ensuring compositional homogeneity on the molecular scale by immobilizing the metal complex in rigid organic polymeric networks.[24] PPM is considered low cost because the synthesis occurs at lower temperatures than those used by conventional techniques (e.g. solid-state reaction).

The starting components may be nitrates, acetates, carbonates among other metals of the desired composition. The metals are dissolved in citric acid to occur chelation of metals, then the ethylene glycol is added to occur polyesterification reaction. After evaporating part of the solvent, the solution is converted into a resin that stores a uniform and homogeneous distribution of the metal cations in the polymer network. Heating the polymeric resin at temperatures above 300 ºC causes a break in the polymer and an appropriate additional heating produces an oxide powder.

1.4 References

1 PHURUANGRAT, A.; THONGTEM, T.; THONGTEM, S. Analysis of lead molybdate and lead tungstate synthesized by a sonochemical method. **Current Applied Physics**, v. 10, n. 1, p. 342-345, 2010. doi:10.1016/j.cap.2009.06.024.

2 YU, S. H. et al. General synthesis of single-crystal tungstate nanorods/nanowires: a facile, low-temperature solution approach. **Advanced Functional Materials**, v. 13, n. 8, p. 639-647, 2003. doi:10.1002/adfm.200304373.

3 YU, P. et al. Preparation and microstructure of $CaMoO_4$ ceramic films prepared through electrochemical technique. **Journal of Electroceramics**, v. 16, p. 473-476, 2006. doi:10.1007/s10832-006-9900-6.

4 WANG, Y. G. et al. Low temperature synthesis of $CaMoO_4$ nanoparticles. **Ceramics International**, v. 33, p. 693-695, 2007. doi:10.1016/j.ceramint.2005.11.003.

5 MIKHAILIK, V. B. et al. Studies of electronic excitations in $MgMoO_4$, $CaMoO_4$ and $CdMoO_4$ crystals using VUV synchrotron radiation. **Physica Status Solidi B**, v. 242 , n. 2, p. 17-19, 2005. doi:10.1002/pssb.200409087.

6 CHOI, G. K. et al. Microwave dielectric properties of scheelite (A = Ca, Sr, Ba) and wolframite (A = Mg, Zn, Mn) $AMoO_4$ compounds. **Journal of the European Ceramic Society**, v. 27, n. 8-9, p. 3063-3067, 2007. doi:10.1016/j.jeurceramsoc.2006.11.037.

7 ZHANG, Z. J. et al. Preparation and luminescent properties of $Eu^{3+}$and Tb^{3+}ions in the host of $CaMoO_4$. **Materials Science and Engineering B**, v. 145, p. 34-40, 2007. doi:10.1016/j.mseb.2007.09.091.

8 SHARMA, N. et al. Carbon-coated nanophase $CaMoO_4$ as anode material for Li ion batteries. **Chemistry of Materials**, v. 16, n. 3, p 504-512, 2004. doi:10.1021/cm0348287.

9 BELOGUROV, S. et al. $CaMoO_4$ scintillation crystal for the search of ^{100}Mo double beta decay. **IEEE Transactions on Nuclear Science**, v. 52, n. 4, p. 1131-1135, 2005. doi:10.1109/TNS.2005.852678.

10 ZHOU, Y. X. et al. Hierarchical $FeWO_4$ microcrystals: solvothermal synthesis and their photocatalytic and magnetic properties. **Inorganic Chemistry**, v. 48, n. 3, p. 1082-1090, 2009. doi:10.1021/ic801806r.

11 SCZANCOSKI, J. C. et al. Morphology and blue photoluminescence emission of $PbMoO_4$ processed in conventional hydrothermal. **Journal of Physical Chemistry C**, v. 113, n. 14, p. 5812-5822, 2009. doi:10.1021/jp810294q.

12 CUI, X. J. et al. Selective synthesis and characterization of single-crystal silver molybdate/tungstate nanowires by a hydrothermal process. **Chemistry European Journal**, v. 10, n. 1, p. 218-223, 2004. doi:10.1002/chem.200305429.

13 ZHANG, Y. M. et al. Synthesis of crystalline $SrMoO_4$ nanowires from polyoxometalates. **Solid State Communications**, v. 133, n. 12, p. 759-763, 2005. doi:10.1016/j.ssc.2005.01.016.

14 CHENG, Y. et al. Evolution of single crystalline dendrites from nanoparticles throught oriented attachment. **Journal of Physical Chemistry B**, v. 109, n. 2, p. 794-798, 2004. doi:10.1021/jp0460240.

15 SHI, H. T. et al. Architectural control of hierarchical nanobelt superstructures in catanionic reverse micelles. **Advanced Functional Materials**, v. 15, n. 3, p. 442-450, 2005. doi:10.1002/adfm.200400242.

16 CAVALCANTE, L. S. et al. Electronic structure, growth mechanism and photoluminescence of $CaWO_4$ crystals. **Crystal Engineering Communications**, v. 14, p. 853-868, 2012. doi:10.1039/c1ce05977g.

17 GONÇALVES, R. F et al. Rietveld refinement, cluster modelling, growth mechanism and photoluminescence properties of CaWO4:Eu3+ microcrystals. **Crystal Engineering Communications**, v. 17, n. 7, p. 1654-1666, 2015. doi:10.039/C4CE02279C.

18 LIU, X. et al. Controllable synthesis of uniform CaMoO4:Eu3+, M+ (M = Li, Na, K) microspheres and optimum luminescence properties. **RSC Advances**, v. 5, p. 9441-9454, 2015. doi:10.1039/c4ra12183j.

19 Diamond - Crystal and Molecular Structure Visualization.Crystal Impact - Dr. H. Putz & Dr. K. Brandenburg GbR, Kreuzherrenstr. 102, 53227 Bonn, Germany http://www.crystalimpact.com/diamond.

20 SAHMI, A. et al. Photoelectrochemical properties of $CaWO_4$ synthetized by chemical route. Application to the phenobarbital electro-photocatalysis. **Journal of Photochemistry and Photobiology A,** v. 349, p. 36-41, 2017. doi:10.1016/j.jphotochem.2017.08.070.

21 PARHI, P.; KARTHIK, T. N.; MANIVANNAN, V. Synthesis and characterization of metal tungstates by novel solid-state metathetic approach. **Journal of Alloys and Compounds**, v. 465, n. 1-2, p. 380-386, 2008. doi:10.1016/j.jallcom.2007.10.089.

22 SHANDILYA, M., RAI, R., SINGH, J. Review: hydrothermal technology for smart materials. **Advances in Applied Ceramics**, v. 115, n. 5, p. 354-376, 2016. doi:10.1080/17436753.2016.1157131.

23 BILECKA, I.; NIEDERBERGER, M. Microwave chemistry for inorganic nanomaterials synthesis. **Nanoscale**, v. 2, p. 1358-1374, 2010. doi:10.1039/b9nr00377k.

24 MARQUES, A. P. A. et al. Effect of the order and disorder of $BaMoO_4$ powders in photoluminescent properties. **Journal of Fluorescence**, v. 18, p. 51-59, 2008. doi:10.1007/s10895-007-0237-6.

2 OBJECTIVES

2.1 General objectives

To synthesize ABO_4 (A = Ca, Ba and B = W, Mo) powders by microwave assisted hydrothermal system (MAH) and polymeric precursor method (PPM) and to study the structural, catalytic and photoluminescent properties of these materials.

2.2 Specific objectives

The purpose of the study reported in paper 1 was to investigate $BaMoO_4$ and $BaWO_4$ powders and the paper 2 was $CaWO_4$ powders. The samples were obtained by MAH and PPM methods and characterized by XRD, FEG-SEM, XANES and EXAFS measurements at the W LIII- and Mo K-edges, UV-Vis spectroscopy, PL measurements. These materials were employed as solid catalysts towards gas phase toluene oxidation reactions to demonstrate their applications.

The paper 3 aimed to obtain $CaMoO_4$ powders by MAH and PPM, to characterize by XRD, FEG-SEM, micro-Raman, XANES and EXAFS measurements at the Mo K-edge. $CaMoO_4$ powders did not present significant catalytic activity to be reported in this paper.

Paper 1 – Published by Ceramics International (doi.org/10.1016/j.ceramint.2016.12.096)

Tittle: Preparation, characterization and catalytic application of Barium molybdate ($BaMoO_4$) and Barium tungstate ($BaWO_4$) in the gas-phase oxidation of toluene.

Paper 2 – Published by Materials Research (doi.org/10.1590/1980-5373-MR-2017-0961)

Tittle: Effect of different synthesis methods on the textural properties of calcium tungstate ($CaWO_4$) and its catalytic properties in the toluene oxidation

Paper 3- Submitted to Materials Science and Engineering B

Tittle: Short- and long-range structural characterization of $CaMoO_4$ powders prepared by microwave assisted hydrothermal and polymeric precursor methods

3 PAPER 1

Preparation, characterization and catalytic application of Barium molybdate ($BaMoO_4$) and Barium tungstate ($BaWO_4$) in the gas-phase oxidation of toluene

Lorena D. S. Alencar[a*], Alexandre Mesquita[b], Carlos A. C. Feitosa[c], Rosana Balzer[d], Luiz F. D. Probst[d], Daniel C. Batalha[e] , Marcelo G. Rosmaninho[e], Humberto V. Fajardo[e] and Maria I. B. Bernardi[a]

[a.] Instituto de Física de São Carlos, Universidade de São Paulo, USP, 13563-120, São Carlos, SP, Brazil.

[b.] Instituto de Geociências e Ciências Exatas, Unesp - Universidade Estadual Paulista, Departamento de Física, 13506-900, Rio Claro, SP, Brazil.

[c.] Departamento de Física, Centro de Ciências Exatas e Tecnologia, Universidade Federal do Maranhão, 65080-805, São Luis, MA, Brazil.

[d.] Departamento de Química, Universidade Federal de Santa Catarina, 88040-900, Florianópolis, SC, Brazil.

[e.] Instituto de Ciências Exatas e Biológicas, Departamento de Química, Universidade Federal de Ouro Preto, 35400-000, Ouro Preto, MG, Brazil.

[*]Corresponding authors. Tel : +55 16 3373 9828. E-mail address : fisicalorenaa@usp.br

Abstract: Barium molybdate and Barium tungstate are important materials due their photoluminescent properties and they also have catalysis and photocatalysis applications. In this work, powders of these compounds were prepared by microwave-assisted hydrothermal (MAH) method and polymeric precursor method (PPM) and their structural and optical properties were studied. Furthermore, these materials were employed as solid catalysts towards gas phase toluene oxidation reactions. X-ray diffraction confirms the purity of materials at both preparation methods and reveals a preferential growth when the powders are prepared by MAH due polymeric agents and processing using microwave, which was confirmed by Field emission scanning electron microscopy. Photoluminesce emission was attributed to the charge-transfer transitions within the $[WO_4]^{2-}$ and $[MoO_4]^{2-}$ complexes. The H_2 Temperature-Programmed Reduction (H_2-TPR), O_2-chemisorption and extended X-ray absorption fine structure (EXAFS) results indicated that $BaWO_4$ samples, compared with $BaMoO_4$ samples, have higher oxygen mobility and oxygen vacancies that appear as key factors for the achievement of better catalytic performances.

Keywords: $BaMoO_4$, $BaWO_4$, Microwave-assisted hydrothermal, Polymeric precursor.

3.1 Introduction

Due to their attractive luminescence Barium molybdate ($BaMoO_4$) and Barium tungstate ($BaWO_4$) are important materials in the electrooptical industry.[1] They present general formula $BaXO_4$ (where X = Mo, W) and a scheelite-type tetragonal structure at room temperature. Belonging to the d^0 compounds with average wide gaps, these materials also can be envisaged as catalysts and photocatalysts either pure or doped.[1]

Various methods of synthesis have been used in the preparation of these compounds,[2-6] among these methods microwave-assisted hydrothermal (MAH) method and polymeric precursor method (PPM) were chosen for their synthesis in the present study.

In microwave-assisted hydrothermal method, molybdates and tungstates with scheelite-type structure are synthesized with high frequency electromagnetic radiation interacting with the permanent dipole of the solvent, which initiates a rapid heating from the resultant molecular rotation.[7] This reaction occurs in closed isolated system conditions, it is performed at pressures greater than 1 atm and temperatures above the boiling point of solvents, reducing the processing time to minutes. Therefore, microwave-assisted hydrothermal method is environmentally friendly and saving energy.

Polymeric precursor method also presents significant efficiency in obtaining multi-component oxides; this process ensures the compositional homogeneity at the molecular scale due the immobilization of the metal complexes in rigid organic polymeric networks, which can reduce the metal segregation. The cation distribution throughout the entire gel system is of fundamental importance for the synthesis of multi-component oxides since the chemical homogeneity often determines the compositional homogeneity of the material.[8] Polymeric precursor method is considered

low cost because the synthesis occurs at lower temperatures than those used by conventional techniques (e.g. solid-state reaction).

Thus, in this paper we report the preparation of $BaMoO_4$ and $BaWO_4$ samples by MAH and PPM methods and their characterization. These materials were employed as solid catalysts towards gas phase toluene oxidation reactions to demonstrate their applications. Volatile organic compounds (VOCs), such as toluene, can be harmful to the environment and human health. So, it is desirable to control the emissions of these pollutants. Catalytic abatement of VOCs has been one of the emergent technologies, mainly because of the high degradation efficiency, even in effluents with low concentrations of VOCs, and low energy cost involved.[9-11]

3.2 Experimental

3.2.1 Synthesis and processing of $BaWO_4$ and $BaMoO_4$ powders by microwave-assisted hydrothermal method

Under continuous stirring and heating between 70 and 90 °C, it was added to 5 x 10^{-3} mol of barium nitrate [$Ba(NO_3)_2$] (99% purity, Sigma-Aldrich) in 40 mL of distilled water. In another beaker, 5 x 10^{-3} mol of sodium tungstate dihydrate [Na_2O_4W-$2H_2O$] (99% purity, Sigma-Aldrich) or sodium molybdate dihydrate [$MoNa_2O_4$-$2H_2O$] (99% purity, Sigma-Aldrich) was diluted in 40 mL distilled water. After complete dissolution of the reagents, the solutions were mixed, and then 15 mL of ethylene glycol (EG) (99%, Synth) were added. For better dissolution of the reagents, the hydrolysis rate of system was increased adjusting the pH to 11 with the addition of 5 mL of NH_4OH (27% in NH_3, Synth). The solution remained stirring for 30 minutes. In the sequence, the solution was transferred to an autoclave and this was coupled to a microwave oven (2.45 GHz, maximum power of 800 W). The processing

occurred at a temperature of 140 °C for 30 minutes and the heating rate was set at 25 °C.min^{-1}. The pressure into the autoclave was stabilized at 0.34 MPa. At the end of the microwave processing, the autoclave was cooled at room temperature. The obtained suspensions were washed several times with distilled water to remove the EG and the NH_4OH, until to neutralize the pH solution (≈ 7) and the last wash was performed with isopropyl alcohol. The powders were dried at 80 °C for 8 hours.

3.2.2 Synthesis of $BaWO_4$ and $BaMoO_4$ powders by polymeric precursor method

To obtain $BaWO_4$ powders, in 100 mL of distilled water under constant stirring and heating of approximately 70 °C was added 2.6 x 10^{-2} mol of tungstic acid [H_2WO_4] (99% purity, Aldrich) and 10 mL of NH_4OH (27% in NH_3, Synth) to adjust the pH of the solution (≈ 11) for complete dissolution of the tungstic acid. In another beaker, citric acid [$C_6H_8O_7$] (99.5% purity, Synth) was dissolved in 100 mL of distilled water under the same conditions of temperature and stirring. This was added to the initial solution of tungstic acid, obtaining a limpid solution (tungsten citrate). The stoichiometry between citric acid/metal used was 3:1 (molar ratio) and the molar ratio between metal cations was 1:1. Thereafter, 2.6 x 10^{-2} mol of barium nitrate [$Ba(NO_3)_2$] (99% purity, Sigma-Aldrich) was diluted in 100 mL of distilled water and added to the tungsten citrate. EG in a proportion (weight) citric acid/EG of 60:40 was added to promote polyesterification of the complex.

$BaMoO_4$ powders were prepared following the same procedure used for the preparation of barium tungstate. The stoichiometry and reagents used were 3.4 x 10^{-2} mol of molybdenum trioxide [MoO_3] (99.5% purity, Merck) and barium carbonate [$BaCO_3$] (99.8% purity, Alfa-Aesar). However, after adding the Ba precursor, it was

necessary to adjust the pH to between 2 and 3 with nitric acid [HNO_3] (65%, Synth) to avoid precipitation of the reagents. Then, EG was added.

The solutions were kept under constant stirring in a temperature range of 150 to 200 °C to occur the polyesterification reaction and evaporation of the excess water, obtaining clear and homogeneous resins.

The polymer resins were calcined at 300 °C for 4 hours at a heating rate of 10 °C/min in ambient atmosphere, obtaining a material with porous structure due to partial decomposition of the polymer and consequent release of gas. The material obtained was deagglomerated in a mortar. The powders were calcined at 700 °C for 2 hours, at a heating rate of 10 °C.min^{-1} in ambient atmosphere.

3.2.3 Sample characterizations

$BaWO_4$ and $BaMoO_4$ powders were structurally characterized by X-ray diffraction (XRD) patterns recorded using a RIGAKU - ULTIMA IV X-Ray with Cu-Kα radiation (λ = 1.5406 Å) in the 2θ range from 20° to 80° with a scanning rate of 0.02°/min. Field emission scanning electron microscopy (FEG-SEM) Zeiss – Sigma was employed to verify the morphology of these powders. X-ray absorption near edge spectroscopy (XANES) and extended X-ray absorption fine structure (EXAFS) measurements at the W LIII- and Mo K-edges of $BaWO_4$ and $BaMoO_4$ samples were collected in transmission mode as a function of the temperature using a Si(111) channel-cut monochromator at the LNLS (National Synchrotron Light Laboratory) facility. The extraction and fit of the EXAFS spectra were performed using the multi-platform applications for X-ray absorption (MAX) software package[12] and theoretical spectra were obtained using the FEFF9 code.[13] UV-Visible spectroscopy was taken with a Varian Cary - 5G. Photoluminescence (PL) spectra were taken with a

Coherent Innova, with a wavelength excitation 350 nm generated by krypton ion laser with adjustable output power of 200 mW to 800 mW, the width of the slit in the monochromator used is 200 nm. PL measurements were performed using a Monospec 27 monochromator (Thermal Jarrel-Ash) coupled to a R446 photomultiplier (Hamatsu Photonics) compound of a lock-in SR-530. All the above measurements were performed at room temperature. The H_2 Temperature-Programmed Reduction (H_2-TPR) was performed using a Quantachrome ChemBET-3000 instrument equipped with a thermal conductivity detector. Prior to the analysis 100 mg of the sample were packed into a quartz cell, heated for 2 h at 200 °C under a He stream and then cooled to room temperature. The experiments were performed between 25 and 950 °C in a flow of 8% H_2/N_2, the temperature increasing linearly at a rate of 10°C.min^{-1}. H_2 consumption was obtained from the integrated peak area of the reduction profiles relative to the calibration curve. CuO was used as calibration reference to quantify the total amount of H_2 consumed during the experiments. The O_2-chemisorption measurements were conducted at 600 °C using a ChemBET analyzer (Quantachrome Instruments).

3.2.4 Catalytic Tests

The catalytic oxidation reactions of toluene were performed in a fixed-bed tubular quartz reactor, placed in an oven, under atmospheric pressure. The following conditions were chosen: 0.11 g of catalyst, inlet toluene (>99%,Vetec) concentration 0.7 g.m^{-3} in air, gas flow rate 20 cm^3.min^{-1}, residence time 0.3 s, gas hourly space velocity 12000 h^{-1} and temperature range 50-400 °C. The catalyst was placed in the middle of the reactor with thermocouples located on the top and bottom of the catalyst bed to monitor the reaction temperature. The catalyst was previously activated in situ under air atmosphere at 250 °C for 1 h. The reagent feed was delivered into the reactor

system using a peristaltic pump (Minipuls 3 – Gilson®). The reaction data were collected after at least 2 h on stream at room temperature. The reactant and product mixtures were analyzed with two in-line gas chromatographs equipped with FID and TCD detectors and an HP-5 column. The catalytic activity was expressed as the percent conversion of toluene. The conversion of the toluene was calculated as follows: $C(\%) = \frac{[Q]_{in} - [Q]_{out}}{[Q]_{in}} x100\%$, where C(%) = percentage of toluene conversion, $[Q]_{in}$ = input quantity and $[Q]_{out}$ = output quantity of toluene, according to the chromatograms.

3.3 Results and discussion

3.3.1 X-ray diffraction analysis

Fig. 3.1 shows the XRD patterns of $BaWO_4$ and $BaMoO_4$ powders processed by microwave-assisted hydrothermal method and by polymeric precursor method. The XRD patterns of $BaWO_4$ and $BaMoO_4$ powders obtained by both methods can be indexed to the scheelite-type tetragonal structure with space group $I4_1/a$ and is in agreement with the respective Inorganic Crystal Structure Database (ICSD) N° 16165 for $BaWO_4$ and N° 50821 for $BaMoO_4$. For $BaWO_4$ MAH powders, XRD pattern shows high intensity diffraction peaks, related to crystallographic planes (020), (220) and (033) indicating the preferential growth in these plans, the same happens for the XRD patterns of the $BaMoO_4$ MAH powders, where the crystallographic planes (020), (220) and (003) have preferred directions. No diffraction peaks related to secondary phase were detected. X-ray patterns confirm phase purity for materials at both preparation methods.

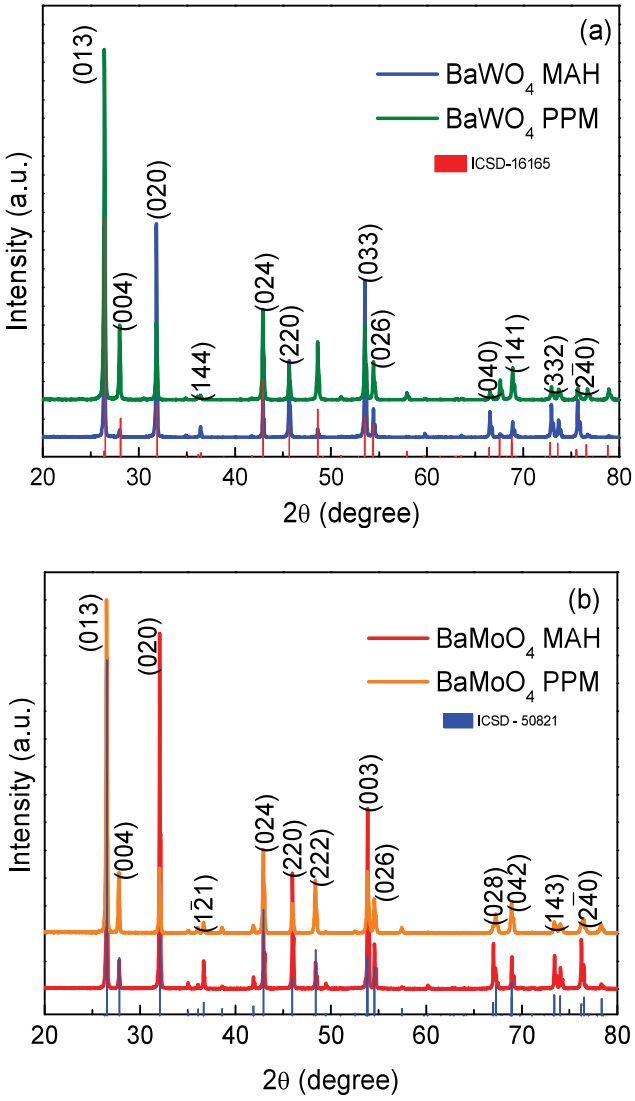

Figure 3.1. XRD patterns of (a) $BaWO_4$ and (b) $BaMoO_4$ powders obtained by MAH and PPM.
Source: By the author

3.3.2 Scanning electron microscope analysis

From the FEG-SEM micrographs were observed that the $BaWO_4$ PPM (Fig. 3.2a) and $BaMoO_4$ PPM (Fig. 3.2b) powders have rounded shape with agglomerated nature and average diameters of 100 nm. Figures 3.2c and 3.2d show FEG-SEM micrographs of $BaWO_4$ MAH and $BaMoO_4$ MAH powders, respectively. In these figures were observed shuttle-like particles with four prominences in the middle part, with particles sizes between 2 and 50 μm. When prepared without polymeric agents, these powders show octahedral morphology.[14] Besides the effects of polymeric agents,

the type of processing using microwave is also responsible for this morphological change.[5] The anisotropic particle shape justifies the peaks observed in X-ray diffractograms which revealed preferential growth along the planes (020), (220) and (033) for $BaWO_4$ MAH and the planes (020), (220) and (003) for $BaMoO_4$ MAH.

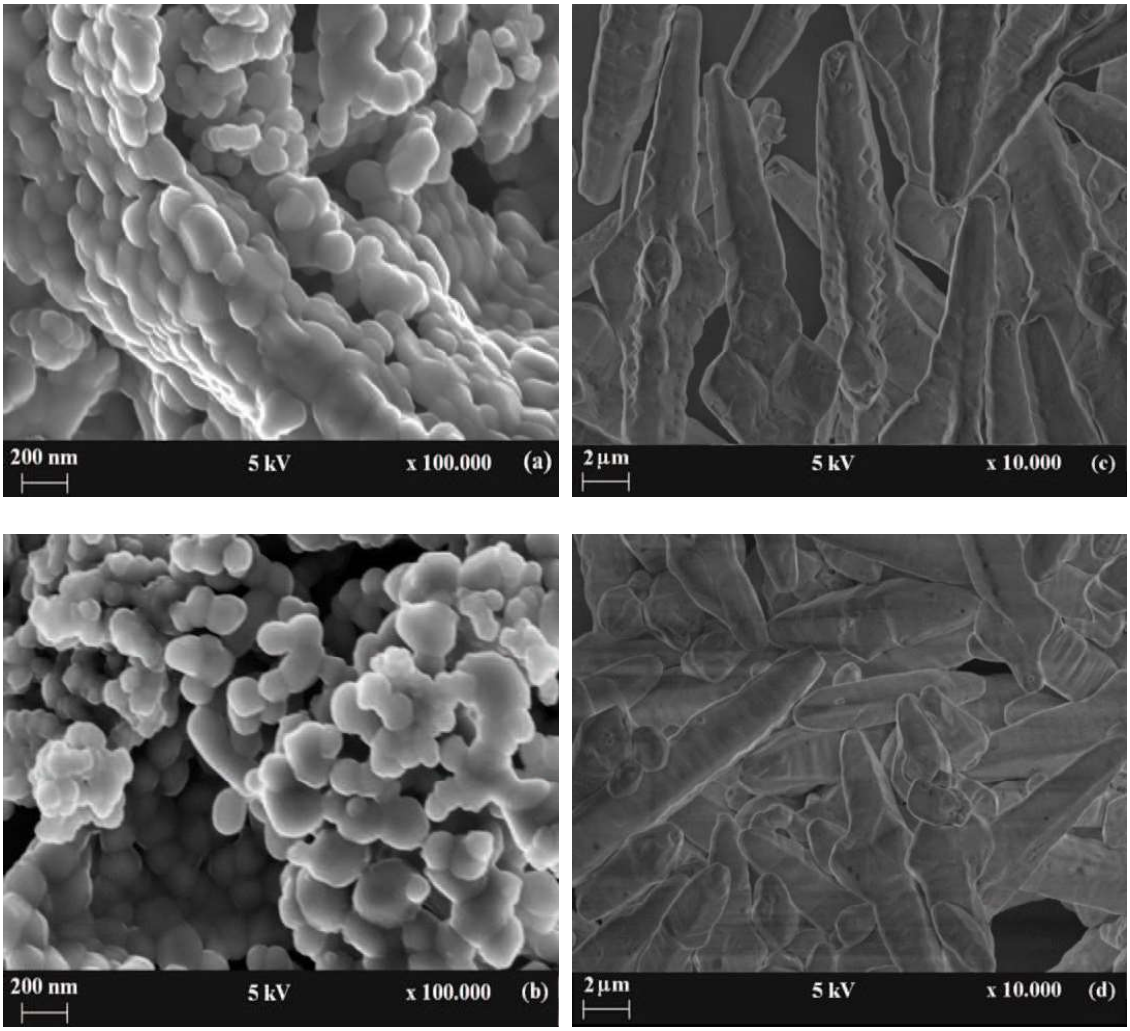

Figure 3.2. FEG-SEM images of (a) $BaWO_4$ and (b) $BaMoO_4$ powders prepared by PPM and (c) $BaWO_4$ and (d) $BaMoO_4$ powders prepared by MAH method.
Source: By the author.

3.3.3 X-ray absorption spectroscopy (XAS) measurements

The structures of the $BaWO_4$ and $BaMoO_4$ samples were also characterized by X-ray absorption spectroscopy (XAS) measurements. XANES spectra provide information on the coordination symmetry and valence of ions incorporated in a solid.

The energy of the absorption edge shifts according to the valence of the absorbing ion, because the binding energy of bound electrons rises as the valence increases. Also, the shape of the absorption edge depends on the unfilled local density of states and the coordination symmetry of the absorbing element. Fig. 3.3a presents the XANES spectra at W L_{III}-edge for $BaWO_4$ samples and the spectrum of a WO_3 standard reference whereas Fig. 3.3b shows the XANES spectra at Mo K-edge for $BaMoO_4$ samples and MoO_3 standard reference.

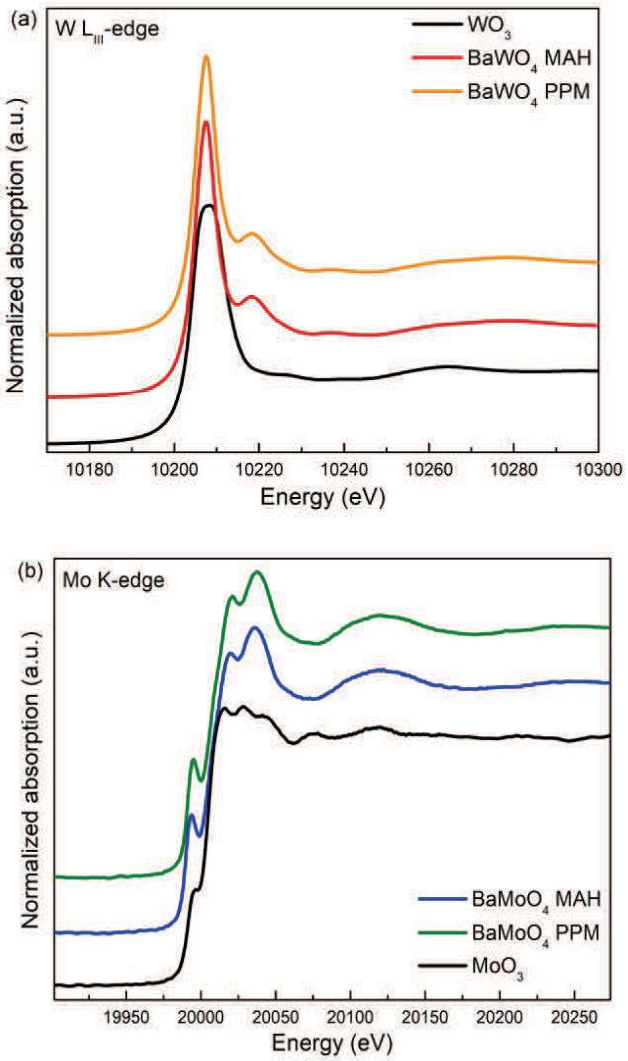

Figure 3.3. XANES spectra at (a) W L_{III}-edge of $BaWO_4$ powders and at (b) Mo K-edge of $BaMoO_4$ powders.

Source: By the author.

The XANES spectra in the W L_{III}-edge of $BaWO_4$ samples, as it can observed in Fig. 3.3a, present different features compared to the XANES spectrum compared of the reference compound (WO_3). In these spectra, the white line mostly derives from electron transitions from the 2*p* 3/2 state to a vacant 5*d* state.[15] As the form and the shape of white line depend on the particular structure, this difference is expected because the WO_3 compound has a W atom in an octahedral environment.[15] We have observed no significant change in these XANES spectra as a function of the preparation method for $BaWO_4$ samples. It can assert that the first coordination shell around tungsten atoms is formed by four oxygen atoms in a quite regular structure independently of the synthesis conditions.[15] The similarity of the post-edge XANES spectra also indicates that second and further coordination shells are quite similar. Similar conclusion can be reached with the observation of Fig. 3.3b, which exhibits the XANES spectra at Mo K-edge for $BaMoO_4$ samples. The pre-edge peaks in XANES spectra of $BaMoO_4$ samples are attributed to the transition from Mo 1*s* states to Mo 4*d*, which is dipole-allowed for tetrahedral symmetry because of the hybridization with O 2*p* states.[16] The same feature results in a shoulder for MoO_3 standard compound, which presents a distorted octahedral coordination.[16] The short-range structural data provided by EXAFS offer an element-specific insight, giving quantitative information about the number, position and identity of atoms surrounding the absorbing element as well as structural disorder within the coordination spheres.

Fig. 3.4 shows the modulus of k^3 weighted Fourier transform of $BaWO_4$ and $BaMoO_4$ samples extracted from W L_{III}- and Mo K-edge EXAFS spectra, respectively.

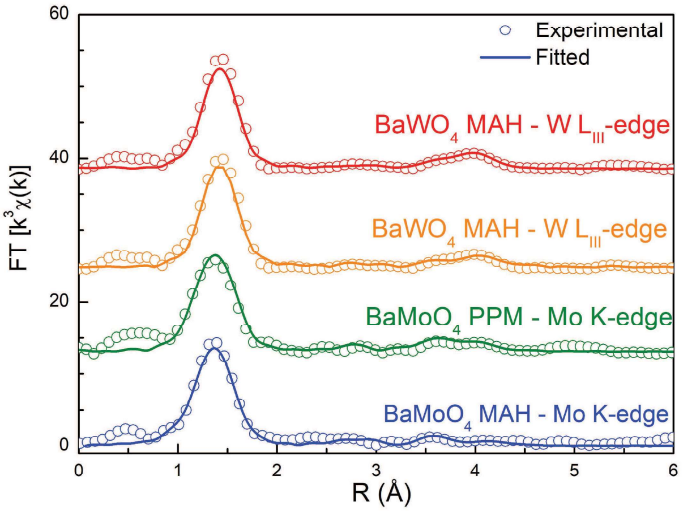

Figure 3.4. Experimental and fitted modulus of k^3 weighted Fourier transform for $BaWO_4$ and $BaMoO_4$ powders at W L_{III}- and Mo K-edge, respectively. Open symbols are experimental data, and solid lines represent fittings using the parameters listed in Table 3.1 and Table 3.2.
Source: By the author.

In order to obtain quantitative information of the local structure around W and Mo atoms, Fourier transform curves were then back Fourier transformed between 1.0 and 2.0 Å to obtain the experimental EXAFS spectra to fit using a theoretical model calculated from the FEFF9 code and crystallographic information according the XRD measurements. In all fits, the number of free parameters was kept smaller than the number of independent points, which is defined as $N_{ind} = 2\Delta R\Delta k/\pi$, where ΔR is the width of the R-space filter windows and ΔK is the actual interval of the fit in the k space.[17] The reliability of the fit, determined by a quality factor (Q), the interatomic distances (R) and Debye–Waller factor (σ^2) relatives to the best fits are shown in Table 3.1 and Table 3.2.

Table 3.1. W L_{III}-edge EXAFS simulation results. R is the distance from the central atom, N is the average coordination number, σ^2 the Debye–Waller factor, and Q the quality factor.

Shell	R (Å)		N		σ^2 (10^{-2} Å^2)		Q	
	MAH	PPM	MAH	PPM	MAH	PPM	MAH	PPM
W-O	1.78(1)	1.78(1)	3.9(4)	3.8(4)	0.04(6)	0.04(5)		
W-O	3.31(3)	3.31(4)	2.9(6)	2.1(8)				
W-Ba	3.94(2)	3.95(3)	3.4(5)	1.8(7)				
W-Ba	4.23(3)	4.23(3)	3.4(2)	1.8(1.1)				
W-W	4.23(3)	4.23(3)	2.7(4)	2.0(1.1)	1.1(2)	0.78(13)	1.34	1.45
W-O	5.5(2)	6.0(3)	1.8(2)	1.0(8)				
W-O	5.9(4)	5.7(4)	0.6(1.5)	0.1(5)				
W-O	4.9(2)	5.3(2)	0.1(1.6)	1.0(3.2)				

Source: By the author.

Table 3.2. Mo K-edge EXAFS simulation results. R is the distance from the central atom, N is the average coordination number, σ^2 the Debye–Waller factor, and Q the quality factor.

Shell	R (Å)		N		σ^2 (10^{-2} Å^2)		Q	
	MAH	PPM	MAH	PPM	MAH	PPM	MAH	PPM
Mo-O	1.72(1)	1.76(2)	3.9(2)	4.1(5)	0.21(4)	0.12(6)		
Mo-O	3.32(5)	3.31(4)	4.7(1.2)	3.7(1.7)				
Mo–Ba	3.87(2)	3.88(3)	4.2(1.1)	3.8(1.6)				
Mo–Ba	4.25(3)	4.20(6)	4.3(1.2)	4.3(1.8)				
Mo–Mo	4.19(4)	4.18(6)	4.0(9)	3.7(1.7)	1.0(2)	0.78(13)	0.78	1.13
Mo–O	4.2(1)	3.9(1)	3.7(7)	3.8(1.9)				
Mo–O	4.4(1)	4.2(2)	3.4(7)	3.6(1.7)				
Mo-O	4.8(1)	4.7(2)	0.0(1.2)	1.8(1.6)				

Source: By the author.

According to the structural model, the absorber atom is surrounded by, in this order, two shells with four O atoms each, two shells with four Ba atoms each, one shell with four W or Mo atoms and three shells with four O atoms each. Thus, the more intense peak, between 1.0 and 2.0 Å in the Fourier transforms, corresponds to a single

scattering interaction between the first four O atoms around the absorber atom. The single scattering interactions relative to W–Ba or Mo-Ba, W-W or Mo-Mo and W-O or Mo-O (beyond the first O neighbors) paths correspond the region observed between 2.0 and 5.0 Å. This region also includes multiple scattering.

The extracted parameters confirm the assumption that preparation method does not introduce high order disorders into the structure. The radial distance (R) for all shells do not change considerably with the preparation method for $BaWO_4$ and $BaMoO_4$ samples. Moreover, we can trace an increase of oxygen vacancies following the average coordination number (N) for the second O-shells. Furthermore, samples prepared by the polymeric precursor method show a lower coordination number in some shells. It can suggest the presence of imperfectness in the crystal lattice. As shown by FEG-SEM micrographs, the average particle size is lower for these samples. Because of this, large amount of the atoms should be placed at the boundary of particles resulting in a lower number of neighbors.[18]

3.3.4 UV-Visible absorption measurements

UV-vis measurements were performed in the diffuse reflectance mode and the optical band gap (E_{gap}) was estimated by method proposed by Kubelka and Munk.[19,20] Fig. 3.5a shows the UV-vis spectra of $BaWO_4$ powders and Fig. 3.5b shows the UV-Vis spectra of $BaMoO_4$ powders processed by MAH and PPM. The insets show the obtained optical band gap for each composition. The E_{gap} values obtained were 5.31 and 5.12 eV for $BaWO_4$ and 4.39 and 4.33 for $BaMoO_4$ prepared by polymeric precursor method and microwave-assisted hydrothermal method, respectively. These values are close those reported in the literature;[1,21-23] the differences in E_{gap} values of the materials studied in this work and of the values observed in the literature may be

related to particle morphology, type of synthesis, time and processing temperature.[4] All these factors result in different structural defects such as oxygen vacancies and distortions on the links, which are capable of promoting the formation of intermediate energy states within the band gap.[24]

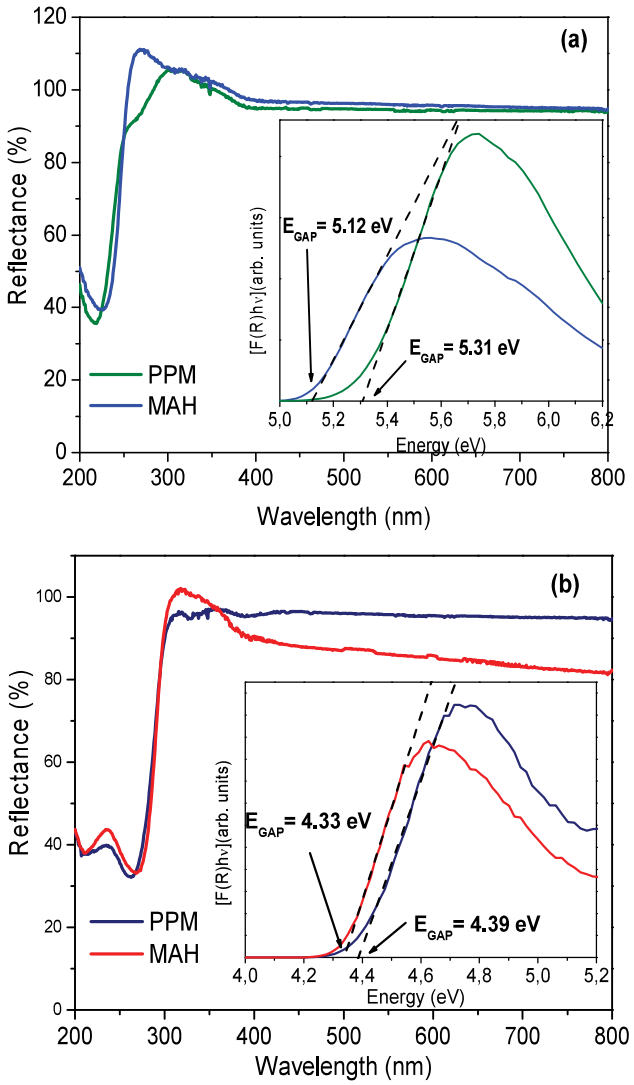

Figure 3.5. UV-vis spectra of (a) $BaWO_4$ powders and (b) $BaMoO_4$ powders processed in a MAH and PPM. The insets show the obtained optical band gap for each composition.
Source: By the author.

The molybdates and tungstates have a typical optical absorption process characterized by direct electronic transitions occurring of maximum energy states located near or in the valence band to minimum energy states located below or in the

conduction band. Due to have fewer intermediate energy levels between the valence band and conduction band these materials have a high E_{gap} value and this value is associated with the degree of order and disorder structural of the materials at an average distance.[25]

3.3.5 PL measurements

Fig. 3.6 shows the PL spectra of $BaWO_4$ and $BaMoO_4$ powders prepared by the two methods proposed in this paper. Photoluminescence spectra show a broad band covering the visible electromagnetic spectrum in the range of 400 to 800 nm, and the profile of the emission band is typical of a multi-fonon and processes at various levels involving the participation of several states within the band gap of the material.[24] The maximum emission peaks are centered on 459 nm and 485 nm for $BaWO_4$, and 491 nm and 498 nm for $BaMoO_4$ prepared by polymeric precursor method and microwave-assisted hydrothermal method, respectively. Values are close to those found in the literature, which is 542 nm to $BaMoO_4$[7] and $BaWO_4$.[25] Both materials prepared by microwave-assisted hydrothermal method show higher emission intensity when compared to materials synthesized by polymeric precursor method. The factors that influence the emission intensity are different such as processing temperature, degree of aggregation and orientation between the particles, variations in particle size distribution, particle morphology and surface defects.[24]

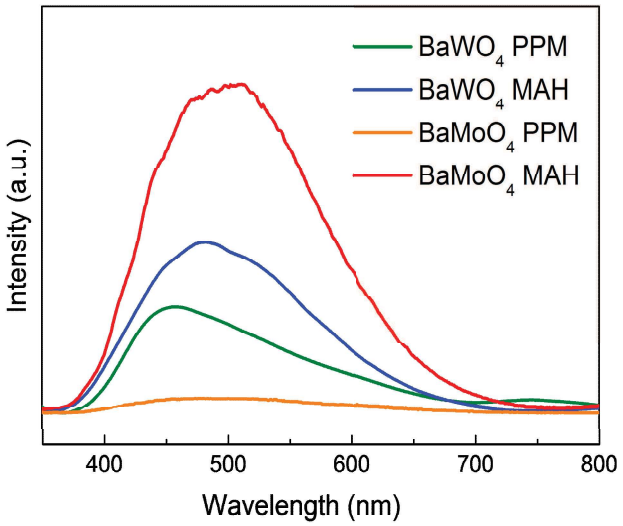

Figure 3.6. PL spectra of $BaWO_4$ and $BaMoO_4$ powders (λ_{EXC} = 350 nm). The maximum emission peaks are centered on 459 nm and 485 nm for $BaWO_4$, and 491 nm and 498 nm for $BaMoO_4$ prepared by MPP and HM, respectively.
Source: By the author.

Some authors suggest that the green photoluminescence band of barium tungstates is due to oxygen vacancies caused by distorted tetrahedral clusters $[WO_4]$[26] and the emission of barium molybdate powders is associated with the existence of distorted $[MoO_3]$ and $[MoO_4]$ clusters, leading to the formation of intermediate energy levels within the band gap. These energy levels are basically compounds of oxygen 2p states (near the valence band) and molybdenum of 4d states (below the conduction band).[27] But in general, these emission spectra are associated to the charge-transfer transitions within the $[WO_4]^{2-}$ and $[MoO_4]^{2-}$ complexes.[21,25,29-30]

3.3.6 H_2-TPR measurements

Fig. 3.7 shows the H_2-TPR profiles of the $BaMoO_4$ and $BaWO_4$ powders. It can be observed different reducibility of the samples according to the synthesis method. The peaks represent the successive reduction steps of the Mo and W species, respectively, since the Ba reduction usually occurs at higher temperatures.

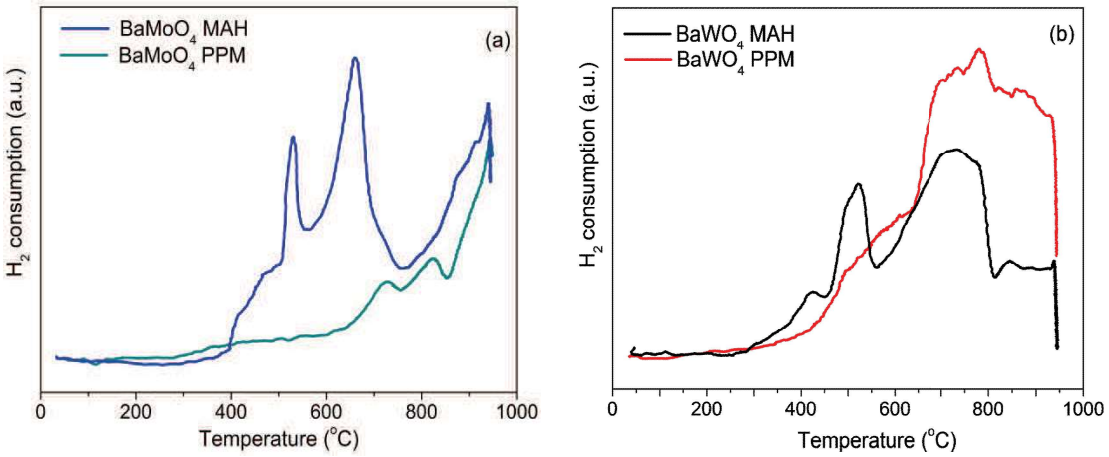

Figure 3.7. H_2-TPR profiles of the catalysts: (a) $BaMoO_4$ powders and (b) $BaWO_4$ powders processed in a MAH and PPM.

Source: By the author.

For both $BaMoO_4$ and $BaWO_4$ produced by microwave assisted hydrothermal method, it can be observed signals at lower temperatures than those of the samples produced by polymeric precursor method. This suggests the presence of more oxidized species in the MAH samples. For the $BaMoO_4$ MAH sample, intense signals at about 530 and 660 °C indicate the presence of high amount of high-oxidized Mo with small particle size dispersion. For $BaMoO_4$ PMM sample it can be observed a broad and with low intensity signal starting at about 300 °C, suggesting the presence of larger particles compared to the $BaMoO_4$ MAH sample. The amount of removable oxygen atoms was considerably smaller for the sample produced by PPM route compared to the MAH material (Fig. 3.8b), in according with the suggested more labile oxygen removable at lower temperature. In the same way, for the $BaWO_4$ samples, the amount of removable oxygen was considerable large for the MAH sample compared to the PPM sample, suggesting a presence of smaller amount of W at the sample. The broader signal for $BaWO_4$ PPM indicates a large distribution of the particle size for this material.

3.3.7 Catalytic activity tests

The synthesized samples were investigated as solid catalysts towards the gas-phase toluene oxidation reaction. Fig. 3.8a shows the toluene conversion as a function of the reaction temperature. The catalysts showed the same tendency, that is, the reagent conversion increased with the increase in the reaction temperature. The only products detected during the experiments were water and carbon dioxide. Without the catalyst, the toluene thermal oxidation started at about 350 °C and achieved only 3% conversion at 500 °C. In the presence of the catalyst, no significant conversion was detected at very low temperatures. The catalysts displayed activities from 150 °C, especially $BaWO_4$ MAH that reached almost 15% of toluene conversion at this temperature. The results showed that the toluene conversion was influenced by the type of catalyst. The $BaWO_4$ samples were more active than $BaMoO_4$ samples presenting the highest conversion levels mainly in the reaction temperatures above 150 °C. The superior oxidation performance of $BaWO_4$ samples can be ascribed to the higher oxygen mobility and concentration of oxygen vacancies, estimated by means of H_2-TPR and O_2-chemisorption measurements (higher hydrogen consumption Fig 3.8b and larger oxygen uptake Fig 3.8c, respectively).[31,32] It can be inferred from Fig. 3.8b that the consumption amount of hydrogen varies from 346.1 $\mu mol.g_{cat}^{-1}$ for $BaWO_4$ MAH, the most active catalyst, to 184.8 $\mu mol.g_{cat}^{-1}$ for $BaMoO_4$ PPM, the less active catalyst. This indicates that the mobile oxygen species available on the $BaWO_4$ MAH surface is larger than that of $BaMoO_4$ PPM.[33] The O_2-chemisorption measurements presented in Fig. 3.8c also support the H_2-TPR analysis. From these values, it can be estimated the total amount of oxygen storage capacity (OSC) available in each catalyst, which is related to the number of oxygen vacancies of them. The $BaWO_4$ MAH exhibited the largest OSC (3,69$mmol.m^{-2}$), indicating that this sample has the highest amount of oxygen vacancies.[34]

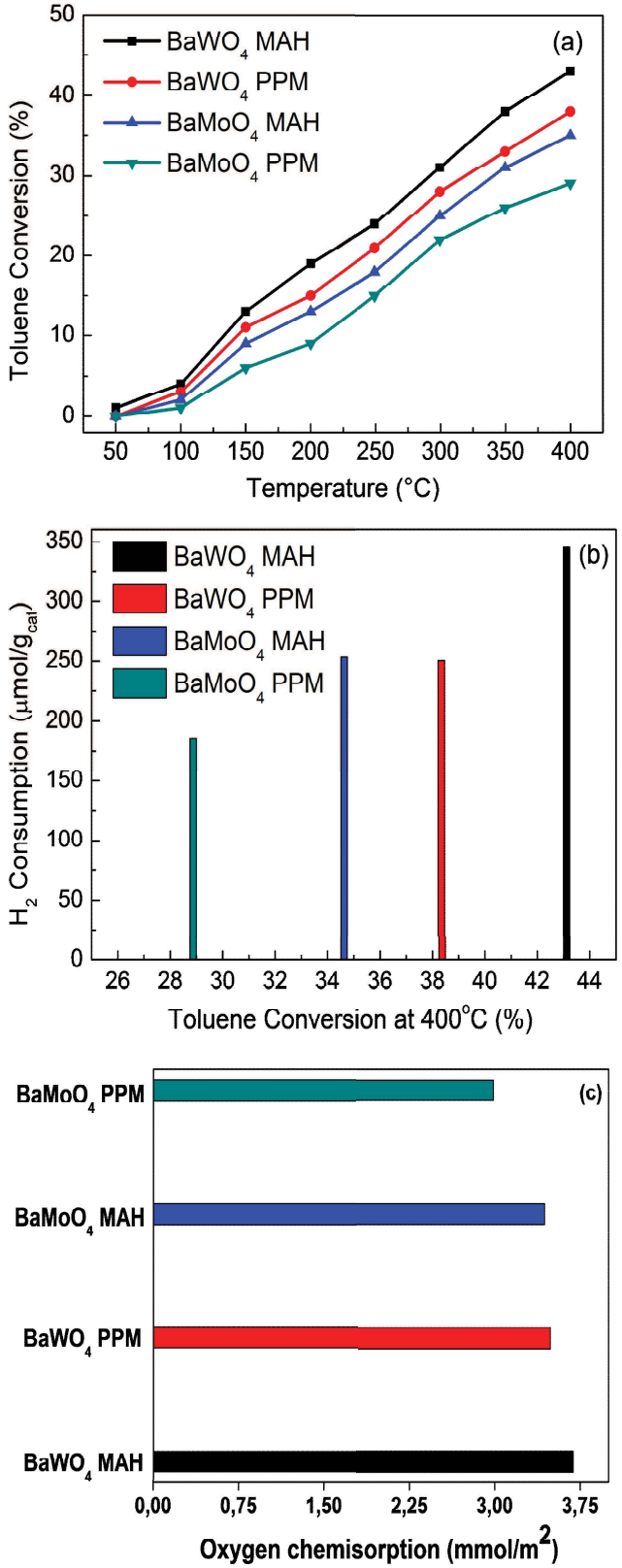

Figure 3.8. (a) Toluene conversion over $BaWO_4$ and $BaMoO_4$ samples as a function of reaction temperature and (b) H_2 consumption from TPR measurements versus catalyst activity at 400 °C and (c) oxygen storage capacity (OSC) from the oxygen chemisorption measurements for each catalyst.

Source: By the author.

The bulk and surface oxygen mobility that can be enhanced by oxygen vacancies play an important role in hydrocarbon oxidation reactions where the oxidation-reduction cycles determine the activity of the catalyst. It is commonly accepted that hydrocarbon oxidation reactions promoted by metal oxides follow a Mars-van Krevelen mechanism in which the solid oxidizes the substrate and the key steps are the supply of oxygen by the reducible oxide surface and the reoxidation of the reduced solid by the oxygen-containing gaseous phase. Oxygen vacancies on the catalyst surface can act accelerating the adsorption and dissociation of gas-phase oxygen molecules resulting in the formation of highly active O-species (e.g., $O_2^-; O_2^{2-}; O^-$) that could be consumed by the organic compound. These vacancies are filled by the oxygen atoms that diffuse from the bulk to the surface of the catalyst or by di-oxygen in the air stream during the process. Thus abundant mobility of active lattice oxygen species enhanced by oxygen vacancies improves the catalytic activity in the toluene oxidation.[34-39]

Table 3.3 shows the light-off temperature (T30, approximate temperature for the 30% toluene conversion) for toluene oxidation over the most active catalyst in the present study ($BaWO_4$ MAH) and some catalysts used in previous investigations.[40-44] It can be observed that the performance of the $BaWO_4$ MAH catalyst is comparable or superior to those of some catalysts reported in the literature, including noble metal based catalysts which are preferred for this process.[45] Although the data presented in this table have been reported using different reaction conditions, and therefore, the comparison between the catalytic behaviors must be done with precaution, they are useful to give us an idea of the good catalytic potential of the samples prepared in the present study.

Table 3.3. Oxidation of toluene over $BaWO_4$ MAH catalyst and other catalysts reported in literature.

Catalyst	T_{30} (°C)	Reference
$BaWO_4$ MAH [a]	290	This study
1.5wt.%Au/Co_3O_4 [b]	150	[40]
1.5wt.%Au/MgO [b]	295	[40]
1wt.%Au/TiO_2 [c]	348	[41]
0.5wt.%Pd-1wt.%Au/TiO_2 [c]	200	[41]
Cu-Mn/Al [d]	265	[42]
β-MnO_2 [e]	275	[43]
Au/β-MnO_2 [e]	220	[43]
1wt.%Au/TiO_2 [f]	325	[44]
1wt.%Au(shell)-0.5wt.%Pd(core)/TiO_2 [f]	275	[44]

a. Gas mixture: 199ppmv in in air, catalyst mass: 0.11g.

b. Gas mixture: 146ppmv in in synthetic gas (O_2, 10 vol.%; N_2, balance), catalyst mass: 0.10g.

c. Gas mixture: 1000ppmv in in air, catalyst mass: 0.10g.

d. Gas mixture: 1000ppmv in in air, catalyst mass: 0.225g.

e. Gas mixture: 2000ppmv in in air, catalyst mass: 0.20g.

f. Gas mixture: 1000ppmv in in air, catalyst mass: 0.10g.

3.4 Conclusions

$BaWO_4$ and $BaMoO_4$ powders were successfully synthesized by microwave-assisted hydrothermal method and by polymeric precursor method. XRD patterns showed that the $BaWO_4$ and $BaMoO_4$ powders have a scheelite-type tetragonal structure with space group $I4_1/a$, without diffraction peaks related to secondary phase. SEM-FEG micrographs showed that $BaWO_4$ and $BaMoO_4$ powders prepared by the polymeric precursors method present rounded shape with agglomerated nature while $BaWO_4$ and $BaMoO_4$ powders prepared by microwave-assisted hydrothermal method present shuttle-like crystals with four prominences in the middle part, with polydisperse particles sizes distribution due polymeric agents and processing using microwave. From the EXAFS results we could state that the $BaWO_4$ samples present increased the content of oxygen vacancies relative to the $BaMoO_4$ samples. The E_{gap}

value was associated with the degree of structural order and disorder of the materials at an average distance. PL emission at room temperature was attributed to the the charge-transfer transitions within the $[WO_4]^{2-}$ and $[MoO_4]^{2-}$ complexes. The H_2-TPR, O_2-chemisorption and EXAFS results indicated that $BaWO_4$ samples, compared with $BaMoO_4$ samples, have higher oxygen mobility and oxygen vacancies that appear as key factors for the achievement of better catalytic performances.

ACKNOWLEDGEMENTS

The authors gratefully acknowledge the financial support of the Brazilian research funding agencies FAPESP/CEPID (grant nos. 13/07909-4 and 13/07296-2), FAPEMIG, CAPES and CNPq. The research was partially carried out at LNLS National Laboratory of Synchrotron Light (proposal number XAFS1 - 19058), Brazil.

3.5 References

1 AFANASIEV, P. Molten salt synthesis of barium molybdate and tungstate microcrystals. **Materials Letters**, v. 61, p. 4622-4626, 2007. doi:10.1016/j.matlet.2007.02.061.

2 PARHI, P.; KARTHIK, T. N.; MANIVANNAN, V. Synthesis and characterization of metal tungstates by novel solid-state metathetic approach. **Journal of Alloys and Compounds**, v. 465, n. 1-2, p. 380-386, 2008. doi:10.1016/j.jallcom.2007.10.089.

3 RANGAPPA, D. et al. Fabrication of AMO_4 (A = Ba, Sr, Ca M= Mo, W) films on M substrate by solution reaction assisted ball rotation. **Journal of Electroceramics**, v. 17, p. 853-860, 2006. doi:10.1007/s10832-006-0459-z.

4 LIM, C. S. Solid-state metathetic synthesis of $BaMO_4$ (M = W, Mo) assisted by microwave irradiation. **Journal of Ceramic Processing Research**, v. 12, n. 5, p. 544-548, 2011.

5 MARQUES, A. P. A. et al. Effect of the order and disorder of $BaMoO_4$ powders in photoluminescent properties. **Journal of Fluorescence**, v. 18, p. 51-59, 2008. doi:10.1007/s10895-007-0237-6.

6 CAVALCANTE, L. S. et al. Growth mechanism of octahedron-like $BaMoO_4$ microscrystals processed in microwave-hydrothermal: Experimental observations and computational modeling. **Particuology**, v. 7, p. 353-362, 2009. doi:10.1016/j.partic.2009.05.002.

7 CAVALCANTE, L. S. et al. $BaMoO_4$ powders processed in domestic microwave-hydrothermal: synthesis, characterization and photoluminescence at room temperature. **Journal of Physics and Chemistry of Solids**, v. 69, p. 2674-2680, 2008. doi:10.1016/j.jpcs.2008.06.107.

8 MAURERA, M. A. M. A. et al. Microstructural and optical characterization of $CaWO_4$ and $SrWO_4$ thin films prepared by a chemical solution method. **Materials Letters**, v. 58, p. 727-732, 2004. doi:10.1016/j.matlet.2003.07.002.

9 HUANG, H. et al. Low temperature catalytic oxidation of volatile organic compounds: a review. **Catalysis Science and Technology**, v. 5, p. 2649-2669, 2015. doi:10.1039/C4CY01733.

10 KHAN, F. I.; GHOSHAL, A. K. Removal of volatile organic compounds from polluted air. **Journal of Loss and Prevention in the Process Industries**, v.13, n. 6, p. 527-545, 2000. doi: 10.1016/S0950-4230(00)00007-3.

11 WANG, F. et al. Manganese oxides with rod-, wire-, tube-, and flower-like morphologies: highly effective catalysts for the removal of toluene. **Environmental Science and Technology**, v. 46, p. 4034−4041, 2012. doi:10.1021/es204038j.

12 MICHALOWICZ, A. et al. MAX: Multiplatform applications for XAFS. **Journal of Physics: Conference Series**, v. 190, p. 012034 (4), 2009. doi:10.1088/1742-6596/190/1/012034.

13 ANKUDINOV, A. L. et al. Real-space multiple-scattering calculation and interpretation of x-ray-absorption near-edge structure. **Physical Review B**, v. 58, n. 12, p. 7565-7576, 1998. doi:10.1103/PhysRevB.58.7565.

14 LUO, Z. et al. Controlled synthesis of different morphologies of $BaWO_4$ crystals via a surfactant-assisted method. **Journal of Crystal Growth**, v. 300, p. 523-529, 2007. doi:10.1016/j.jcrysgro.2006.12.031.

15 GRACIA, L. et al. Presence of excited electronic state in $CaWO_4$ crystals provoked by tetrahedral distortion: An experimental and theoretical investigation. **Journal of Applied Physics**, v. 110, p. 043501 (11), 2011. doi:10.1063/1.3615948.

16 ROCCA, F. et al. XANES and EXAFS at Mo K-edge in $(AgI)_{1-x}(AgMoO_4)_x$ glasses and crystals. **Solid State Ionics**, v. 121, p. 189-192, 1999.

17 HASNAIN, S. S. Report on the International Workshops on Standards and Criteria in XAFS. **X-ray Absorption Fine Structure**: Proceedings of the VI International Conference on X-ray Absorption Fine Structures, Ellis Horwood, New York, 1991.

18 CURCIO, A. L.; BERNARDI, M. I. B.; Mesquita, A. Local Structure and photoluminescence properties of nanostructured $Zn_{1-x}Mn_xS$ Material. **Physica Status Solidi C**, v. 12, n. 12, p. 1367-1371, 2015. doi:10.1002/pssc.201510135.

19 MORALES, A. E.; MORA, E. S.; PAL, U. Use of diffuse reflectance spectroscopy for optical characterization of un-supported nanostructures. **Revista Mexicana de Física**, v. 53, n. 5, p. 18-22, 2007.

20 KUBELKA, P.; MUNK, F. Ein Beitrag Zur Optik Der Farbanstriche. **Zeitschrift für Technische Physik**, v. 12, p. 593-603, 1931.

21 SCZANCOSKI, J. C. et al. Electronic structure and optical properties of $BaMoO_4$ powders. **Current Applied Physics**, v. 10, p. 614-624, 2010. doi:10.1016/j.cap.2009.08.006.

22 ZAWAWI, S. M. M. et al. Structural and optical characterization of metal tungstates (MWO_4; M = Ni, Ba, Si) synthesized by a sucrose-templated method. **Chemistry Central Journal**, v. 7, p. 80 (10), 2013.

23 SADIQ, M. M. J.; NESARAJ, A. S. Soft chemical synthesis and characterization of $BaWO_4$ nanoparticles for photocatalytic removal of Rhodamine B present in water

sample. **Journal of Nanostructure in Chemistry**, v. 05, p. 45-54, 2015. doi:10.1007/s40097-014-0133-y.

24 LONGO, V. M. et al. Hierarchical assembly of $CaMoO_4$ nano-octahedrons and their photoluminescence properties. **Journal of Physical Chemistry C**, v. 115, p. 5207-5219, 2011. doi:10.1021/jp1082328.

25 CAVALCANTE, L. S. et al. Electronic structure, growth mechanism and photoluminescence of $CaWO_4$ crystals. **Crystal Engineering Communications**, V. 14, p. 853-868, 2012. doi:10.1039/c1ce05977g.

26 CAVALCANTE, L. S. et al. Synthesis, characterization, anisotropic growth and photoluminescence of $BaWO_4$. **Crystal Growth and Design**, v. 09, p. 1002-1012, 2009. doi:10.1021/cg800817x.

27 SINELNIKOV, B. M.; SOKOLENKO, E. V.; ZVEKOV, V. Y. The nature of green luminescence centers in scheelite. **Inorganic Materials**, v. 32, n. 9, p. 999-1001, 1996.

28 CAMPOS, A. B. et al. Mechanisms behind blue, green, and red photoluminesce emissions in $CaWO_4$ and $CaMoO_4$ powders. **Applied Physics Letters**, v. 91, p. 051923 (3), 2007. doi:10.1063/1.2766856.

29 LIU, X. et al. Controllable synthesis of uniform $CaMoO_4:Eu^{3+}$, M^+ (M = Li, Na, K) microspheres and optimum luminescence properties. **RSC Advances**, v. 5, p. 9441-9454, 2015. doi:10.1039/c4ra12183j.

30 RANGAPPA, D. et al. Fabrication of AMO_4 (A = Ba, Sr, Ca M= Mo, W) films on M substrate by solution reaction assisted ball rotation. **Journal of Electroceramics**, v. 17, p. 853-860, 2006. doi:10.1007/s10832-006-0459-z.

31 ILIEVA, L. et al. Gold catalysts on ceria doped with MeO_x (Me = Fe, Mn, Co and Sn) for complete benzene oxidation: effect of composition and structure of mixed supports. **Reaction Kinetics, Mechanisms and Catalysis**, v. 105, n. 1, p. 23-37, 2012. doi:10.1007/s11144-011-0368-2.

32 ZHANG, C. et al. Enhanced oxygen mobility and reactivity for ethanol steam reforming. **Aiche Journal**, v. 58, n. 2, p. 516-525, 2012. doi:10.1002/aic.12599.

33 SUN, G. B. et al. A crucial role of surface oxygen mobility on nanocrystalline Y_2O_3 support for oxidative steam reforming of ethanol to hydrogen over Ni/Y_2O_3 catalysts. **Applied Catalysis B: Environmental**, v. 81, p. 303-312, 2008. doi:10.1016/j.apcatb.2007.12.021.

34 BALZER, R. et al. $Ce_{1-x}Co_xO_2$ nanorods prepared by microwave-assisted hydrothermal method: novel catalysts for removal of volatile organic compounds. **Science of Advanced Materials**, v. 7, n. 7, p. 1406-1414, 2015. doi:10.1166/sam.2015.2059.

35 LI, J. et al. Effect of MnO_2 morphology on the catalytic oxidation of toluene over Ag/MnO_2 catalysts. **Applied Surface Science**, v. 385, p. 234-240, 2016. doi:10.1016/j.apsusc.2016.05.114.

36 CASTAÑO, M. H.; MOLINA, R.; MORENO, S. Oxygen storage capacity and oxygen mobility of Co-Mn-Mg-Al mixed oxides and their relation in the VOC oxidation reaction. **Catalysts**, v. 5, n. 2, p. 905-925, 2015. doi:10.3390/catal5020905.

37 DA SILVA, A. G. M. et al. Efficient ceria-silica catalysts for BTX oxidation: probing the catalytic performance and oxygen storage. **Chemical Engineering Journal**, v. 286, p. 369-376, 2016. doi:10.1016/j.cej.2015.10.097.

38 LIU, Y. et al. Mesoporous Co_3O_4-supported gold nanocatalysts: Highly active for the oxidation of carbon monoxide, benzene, toluene, and o-xylene. **Journal of Catalysis**, v. 309, p. 408-418, 2014. doi:10.1016/j.jcat.2013.10.019.

39 LIOTTA, L. F. et al. Total oxidation of propene at low temperature over Co_3O_4-CeO_2 mixed oxides: Role of surface oxygen vacancies and bulk oxygen mobility in the catalytic activity. **Applied Catalalysis A**, v. 347, p .81-88, 2008. doi:10.1016/j.apcata.2008.05.038.

40 WU, H. et al. Catalytic oxidation of toluene and p-xylene using gold supported on Co_3O_4 catalyst prepared by colloidal precipitation method. **Journal of Molecular Catalysis A: Chemical**, v. 351, p. 188-195, 2011. doi:10.1016/j.molcata.2011.10.005.

41 HOSSEINI, M. et al. Promotional effect of gold added to palladium supported on a new mesoporous TiO_2 for total oxidation of volatile organic compounds. **Catalysis Today**, v. 122, n. 3-4, p. 391-396, 2007. doi:10.1016/j.cattod.2007.03.012.

42 MATĚJOVÁ, L. et al. Total oxidation of model volatile organic compounds over some commercial catalysts. **Applied Catalysis A**, v. 443-444, n. 7, p. 40-49, 2012. doi:10.1016/j.apcata.2012.07.018.

43 YE, Q. et al. Nanosized Au supported on three-dimensionally ordered mesoporous β-MnO_2: Highly active catalysts for the low-temperature oxidation of carbon monoxide, benzene, and toluene. **Microporous and Mesoporous Materials**, v. 172, p. 20-29, 2013. doi:10.1016/j.micromeso.2013.01.007.

44 HOSSEINI, M. et al. Catalytic performance of core-shell and alloy Pd-Au nanoparticles for total oxidation of VOC: The effect of metal deposition. **Applied Catalysis B**, v. 111-112, p. 218-224, 2012. doi:10.1016/j.apcatb.2011.10.002.

45 LIOTTA, L. F. Catalytic oxidation of volatile organic compounds on supported noble metals. **Applied Catalysis B: Environmental,** v. 100, p. 403-412, 2010. doi:10.1016/j.apcatb.2010.08.023.

4 PAPER 2

Effect of different synthesis methods on the textural properties of calcium tungstate ($CaWO_4$) and its catalytic properties in the toluene oxidation

Lorena D. S. Alencar*[1], Naiara A. Lima[1], Alexandre Mesquita[2], Luiz F. D. Probst[3], Daniel C. Batalha[4], Marcelo G. Rosmaninho[4], Humberto V. Fajardo[4], Rosana Balzer[5], Maria I. B. Bernardi[1]

[1.] Instituto de Física de São Carlos, Universidade de São Paulo, USP, 13563-120, São Carlos, SP, Brazil.

[2.] Instituto de Geociências e Ciências Exatas, Unesp, Universidade Estadual Paulista, Departamento de Física, 13506-900, Rio Claro, SP, Brazil.

[3.] Departamento de Química, Universidade Federal de Santa Catarina, UFSC, 88040-900, Florianópolis, SC, Brazil.

[4.] Instituto de Ciências Exatas e Biológicas – Departamento de Química, Universidade Federal de Ouro Preto, UFOP, 35400-000, Ouro Preto, MG, Brazil.

[5.] Departamento de Engenharias e Exatas, Universidade Federal do Paraná, UFPR, 85950-000, Palotina, PR, Brazil.

*Corresponding authors. Tel : +55 16 3373 9828. E-mail address : fisicalorenaa@usp.br

Abstract: Calcium tungstate ($CaWO_4$) crystals were prepared by microwave-assisted hydrothermal (MAH) and polymeric precursor methods (PPM). These crystals were structurally characterized by X-ray diffraction (XRD), N_2 adsorption, X-ray absorption near edge spectroscopy (XANES) and extended X-ray absorption fine structure (EXAFS) measurements. The morphology and size of these crystals were observed by field emission scanning electron microscopy (FE-SEM). Their optical properties were investigated by ultraviolet visible (UV-Vis) absorption and photoluminescence (PL) measurements. Moreover, these materials were employed as catalysts towards gas phase toluene oxidation reaction. XRD indicates the purity of materials for both preparation methods and MAH process produced crystalline powders synthesized at lower temperatures and shorter processing time compared to the ones prepared by PPM. FE-SEM images showed particles with rounded morphology and particles in clusters dumbbells-like shaped. PL spectra exhibit a broad band covering the visible electromagnetic spectrum in the range of 360 to 750 nm. XANES and EXAFS results show that preparation method does not introduce high disorders into the structure, however the H_2-TPR results indicated that the catalyst reducibility is affected by the preparation method of the samples.

Keywords: $CaWO_4$, Toluene, H_2-TPR, XANES, EXAFS.

4.1 Introduction

Calcium tungstate, with formula $CaWO_4$, presents its primitive cell formed by ionic groups Ca^{2+} and WO_4^{2-} characterized by an arrangement of $[CaO_8]$ in a deltahedral coordination and a $[WO_4]$ tetrahedral coordination clusters[1]. It is a versatile material that exhibit thermal and optical properties[2-4] well known in the literature. Catalytic properties of calcium compounds have been studied. For example they have potential applications in catalysis for water oxidation,[5-6] for ethanolysis of vegetable oils[7-8] and for CO_2 and steam carbon gasifications.[9-10]

Several synthesis methods have been developed to obtain $CaWO_4$ crystals: co-precipitation, solvothermal, microwave-hydrothermal,[11-12] electrochemical,[13] aiming to reduce the processing time and temperatures encountered in traditional methods, such as an oxide mixture or solid state reaction. In this paper, $CaWO_4$ powders were synthesized by microwave-assisted hydrothermal (MAH) method and polymeric precursor method (PPM). PPM allows to obtain high-purity homogeneous systems at the molecular scale due the immobilization of the metal cations in a polymeric networks, which can be annealed at relatively low temperatures (700 ºC).[14-15] Microwave-assisted hydrothermal method is able to synthesize inorganic materials, such as tungstates, because the high frequency of the electromagnetic radiation promotes a rapid heating accelerating the chemical reactions.[16-18]

In this work, we present the preparation of $CaWO_4$ samples, through MAH and PPM methods, their characterization and catalytic properties towards gas phase toluene oxidation reaction. The emission of a volatile organic compound (VOC), such as toluene, can be controlled using destruction methods in which they are converted into carbon dioxide and water. In this regard, catalytic oxidation has been one of the most efficient and promising technologies for abatement of these compounds, mainly because of the high degradation efficiency, even in effluents with low concentrations of VOCs, and low energy and costs

involved.[17,19-21] The choice of the suitable catalyst to be applied in the process is difficult due to the variety and nature of the range of mixtures of VOCs.[21] Therefore, this study aimed to contribute to the development of heterogeneous catalysts for this purpose.

4.2 Experimental

Polycrystalline $CaWO_4$ particles were synthesized by microwave-assisted by hydrothermal method (MAH) and polymeric precursor method (PPM).

4.2.1 Synthesis of $CaWO_4$ by microwave-assisted by hydrothermal (CWOH)

Stoichiometric CaN_2O_6-$4H_2O$ (*Sigma-Aldrich*, 99%) and Na_2WO_4-$2H_2O$ (*Sigma-Aldrich*, 99%) were singly dissolved in distilled water at 70 °C and then they were mixed. A desired amount of ethylene glycol (EG) (*Synth,* 99%) was dissolved in the above solution as polymeric reagent (H_2O:EG ratio of 5.3). The pH value of above solution was adjusted to 11 by ammonium hydroxide (*Synth,* 27%) addition in order to increase the system's hydrolysis rate. After the co-precipitation reaction (equations (4.1), (4.2)) the solution was transferred to a Teflon cup and subsequently into the autoclave; this was coupled to the domestic microwave oven (2.45 GHz, maximum power of 800 W). Processing occurred at 140 °C for 30 min and the heating rate was set at 25 °C min^{-1}.

$$Ca(NO_3)_{2\,(aq)} + Na_2WO_{4(aq)} \rightarrow Ca^{2+}{}_{(aq)} + 2\,NO_3^{-}{}_{(aq)} + 2\,Na^{+}{}_{(aq)} + WO_4^{2-}{}_{(aq)} \quad (4.1)$$

$$Ca^{2+}{}_{(aq)} + 2\,NO_3^{-}{}_{(aq)} + 2\,Na^{+}{}_{(aq)} + WO_4^{2-}{}_{(aq)} \rightarrow CaWO_{4\,(s)} + 2Na^{+}{}_{(aq)} + 2NO_3^{-}{}_{(aq)} \quad (4.2)$$

The precipitate formed was washed several times with distilled water, it was centrifuged, and then dried around 80 °C in an oven for about 8 hours to get white powder.

4.2.2 Synthesis of $CaWO_4$ by polymeric precursor method (CWOP)

To prepare $CaWO_4$ powders, 3.5 x 10^{-2} mol of H_2WO_4 (*Aldrich*, 99%) was dissolved in 100 mL of distilled water under constant stirring and heating of approximately 70 °C then the pH of the solution was increased to ≈ 11 by adding 10 mL of NH_4OH (*Synth,* 27% in NH_3,) for complete dissolution of the tungstic acid. Citric acid (*Synth*, 99.5%) was dissolved in 100 mL of distilled water under the same conditions of temperature and stirring, it was added to the initial solution of tungstic acid, obtaining the tungsten citrate. After homogenization, 3.5 x 10^{-2} mol of $Ca(NO_3)_2$-4 H_2O (*Sigma-Aldrich,* 99%) was diluted in 100 mL of distilled water and added to the tungsten citrate. EG in a proportion (weight) citric acid/EG of 60:40 was added to promote polyesterification of the complex (eq. (4.3) - (4.8)). The temperature was raised to 150 to 200 °C in order to promote the polyesterification reaction and evaporation of the excess of water.

The complexation of calcium with citric acid led to the following reactions :

$$Ca(NO_3)_2.\ 4H_2O + 2C_6O_7H_8 \rightarrow Ca(C_6O_7H_7)_2 + 2HNO_3 + 4H_2O \quad (4.3)$$

forming nitric acid and water. The tungsten complexation reaction occurred as follows:

$$H_2WO_{4(aq.)} \xrightarrow{70\ °C} WO_3 + H_2O \quad (4.4)$$

$$WO_3 + H_2O + 2\ NH_4OH \rightarrow W^{2+} + H_2O + 2NH_4^+ + 2OH^- + 3/2\ O_2(g) \quad (4.5)$$

$$W^{2+} + H_2O + 2NH_4^+ + 2OH^- + 2\ C_6O_7H_8 \rightarrow W(C_6O_7H_7)_2 + H_3O^+ + 2NH_4^+ + 2OH^- \quad (4.6)$$

forming ammonium hydroxide and water.

Mixing these metallic complexes (metallic citrates) above 70 °C triggers the onset of the esterification reaction between metal citrate and ethylene glycol, as follows:

$$M^{n+}\,[OCOCH_2C(OH)(COOH)CH_2COOH]_x + 3HOCH_2CH_2OH \rightarrow$$

$$M^{n+}[OCOCH_2C(OH)(COOH)CH_2COOCH_2CH_2OH]_x + xH_2O \quad (4.7)$$

In the compound studied here, the polyesterification reaction occurred continuously until the polymer network was formed. Based on these reactions, the following basic units can be formed in the polymeric network:

$$\{W^{4+}[OCOCH_2C(OCH_2\text{-}\ldots)(COOCH_2\text{-}\ldots)CH_2COOCH_2\text{-}\ldots]_4\}$$

$$\{Ca^{2+}[OCOCH_2C(OCH_2\text{-}\ldots)(COOCH_2\text{-}\ldots)CH_2COOCH_2\text{-}\ldots]_2\} \quad (4.8)$$

The main volatile compounds contained in the resin were H_2O, NH_4OH, HNO_3 and polyester.

The polymer resin was annealed at 300 °C for 4 hours at a heating rate of 10 °C min^{-1} in ambient atmosphere. The material obtained was deagglomerated using an agate mortar and it was annealed at 700 °C for 2 hours, at a heating rate of 10 °C min^{-1} in ambient atmosphere. The molar ratio between metal cations was 1:1 and the molar ratio stoichiometry between citric acid/metal was 3:1.

4.2.3 Samples characterizations

The phase of synthesized samples were characterized by powder X-ray diffraction (XRD) with a RIGAKU - ULTIMA IV X-Ray diffractometer using Cu-Kα (λ = 1.5406 Å) radiation for 2θ values from 20° to 80°. The morphology of the particles was investigated by scanning electron microscope (SEM; Zeiss – Sigma). UV-Visible (UV-Vis) spectroscopy was measured in the range of 200 – 900 nm (Varian Cary - 5G spectrophotometer). Photoluminescence (PL) spectra were obtained on a Monospec 27 monochromator (Thermal Jarrel-Ash) and a R446 photomultiplier (Hamatsu Photonics) compound of a lock-in SR-530 using a wavelength excitation of 350 nm generated by krypton ion laser with adjustable output power of 200 mW to 800 mW. The width of the slit used in the monochromator is 200

μm. All of the above mentioned characterization techniques were carried out at room temperature. Nitrogen adsorption–desorption measurements of the obtained powders were performed at 77 K with an ASAP 2020 - MICROMERITICS adsorption apparatus. The surface areas were determined by Langmuir model in the adsorption data in a relative pressure range of 0.05–0.2. X-ray absorption near edge spectroscopy (XANES) and extended X-ray absorption fine structure (EXAFS) measurements at the W LIII-edge (10203 eV) of $CaWO_4$ samples were collected in transmission mode as a function of the temperature using a Si(111) channel-cut monochromator at the LNLS (National Synchrotron Light Laboratory) facility using the D04B-XAFS1 beam line. The extraction and fit of the EXAFS spectra were performed using the multi-platform applications for X-ray absorption (MAX) software package[22] and theoretical spectra were obtained using the FEFF9 code.[23] Hydrogen temperature programmed reduction (H_2-TPR) analyses were performed in a Quantachrome ChemBET-TPD/TPR, from room temperature to 1100 °C, at 10 °C.min^{-1} heating rate, using a 5%H_2/N_2 mixture (25 mL min^{-1} flow rate) as reducing gas and about 50 mg of sample. The resulting curves were analyzed using Origin 9.0.0 software and the observed peaks were adjusted using Gaussian model.

4.2.4 Catalytic tests

The catalytic oxidation of toluene was carried out, under atmospheric pressure, in a fixed-bed tubular quartz reactor placed in an oven. The tests were performed under the following conditions: 0.11 g of catalyst, inlet toluene (>99%,Vetec) concentration 0.7 g.m^{-3} in air, gas flow rate 20 cm^3.min^{-1}, residence time 0.3 s, gas hourly space velocity 12000 h^{-1} and temperature range 50-350 °C. To monitor the reaction temperature, the catalyst was placed in the middle of the reactor with thermocouples located on the top and bottom of the catalyst bed. The catalyst was previously activated in situ under air atmosphere at 250 °C for 1 h. A

peristaltic pump (Minipuls 3 – Gilson®) was used to deliver the reagent feed into the reactor system. The reaction data were collected after at least 2 hours on stream at room temperature. The reactant and product mixtures were analyzed with two in-line gas chromatographs equipped with FID and TCD detectors and an HP-5 column. The catalytic activity was expressed as the percent conversion of toluene. The conversion of the toluene was calculated as follows: $C(\%) = \frac{[Q]_{in} - [Q]_{out}}{[Q]_{in}} x100\%$, where C(%) = percentage of toluene conversion, $[Q]_{in}$ = input quantity and $[Q]_{out}$ = output quantity of toluene. According to the chromatograms, water and carbon dioxide were the only products detected during the experiments.

4.3. Results and discussion

4.3.1 X-ray diffraction analysis

All the diffraction peaks in Figure 4.1 correspond to the reflections of tetragonal scheelite structure (space group $I4_1/a$) with $CaWO_4$ cell parameters $a = b = 5.243$ Å and $c = 11.376$ Å according to Inorganic Crystal Structure Database (ICSD) card N° 15586. Sharp diffraction peaks indicate the high degree of crystallinity of the powder prepared and no remarkable diffraction peak of other phases can be found in the XRD patterns. These results confirm that the MAH process produced crystalline powders synthesized at low temperatures with shorter processing time when compared to the PPM.

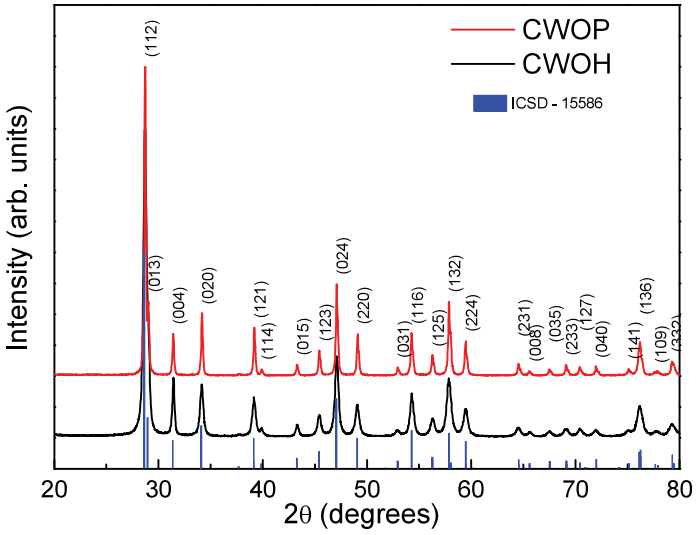

Figure 4.1. XRD patterns of CWOH and CWOH powders.
Source: By the author.

The crystallite sizes of the samples are determined by applying the Debye–Scherrer formula, $D = K\lambda/(\beta\cos\theta)$, where λ is the wavelength of the X-ray radiation, K is a constant taken as 0.9, β is the full width at half-maximum (FWHM) in radian of the main peak, and θ is the diffracting angle.[24] The crystallite sizes are estimated of 45 and 29 nm for CWOP and CWOH, respectively. The crystallite size is related with the processing temperature. CWOH sample was heating at 140 ºC and CWOP sample was annealed at 700 ºC. Observing Table 4.1, it is possible to deduce that elevating heating temperature would favor the crystallite growth.[25-29]

Table 4.1. Comparative results between the crystallite size by Debye–Scherrer formula obtained in this work (*) with those published in the literature. CP = Co-precipitation, PR = Precipitation, MAH = Microwave-assisted hydrothermal, HC = Hydrothermal conventional, SR = Synthetic route, CC = Citrate complex precursor and MPP = Polymeric precursor method.

Method	Temperature (°C)	Crystallite size (nm)	Ref.
CP	80	18	[25]
PR	100	24	[26]
MAH	140	29	*
HC	190	32	[27]
SR	500	33	[28]
CC	500	35	[29]
PPM	700	45	*

Source: By the author.

4.3.2 Field emission scanning electron microscopy analysis

FE-SEM images (Fig. 4.2 (a.b)) show that the polycrystalline powders obtained by PPM are composed of a number of nanosized particles (Fig. 4.2a). These particles are agglomerated with rounded morphology and average diameters of 100 nm. CWOH (Fig. 4.2b) has particles in clusters dumbbells-like shaped. These clusters with recognizable boundaries are constructed from the highly oriented nanoparticles connected with each other during the self-assembly process.[30] The formation of such morphology was reported earlier in tungstates like $SrWO_4$, $CaWO_4$ and $BaWO_4$.[30-33] The possible formation mechanism of this morphology has been proposed by some researchers based on surfactant and polymeric agents under different experimental conditions.[34]

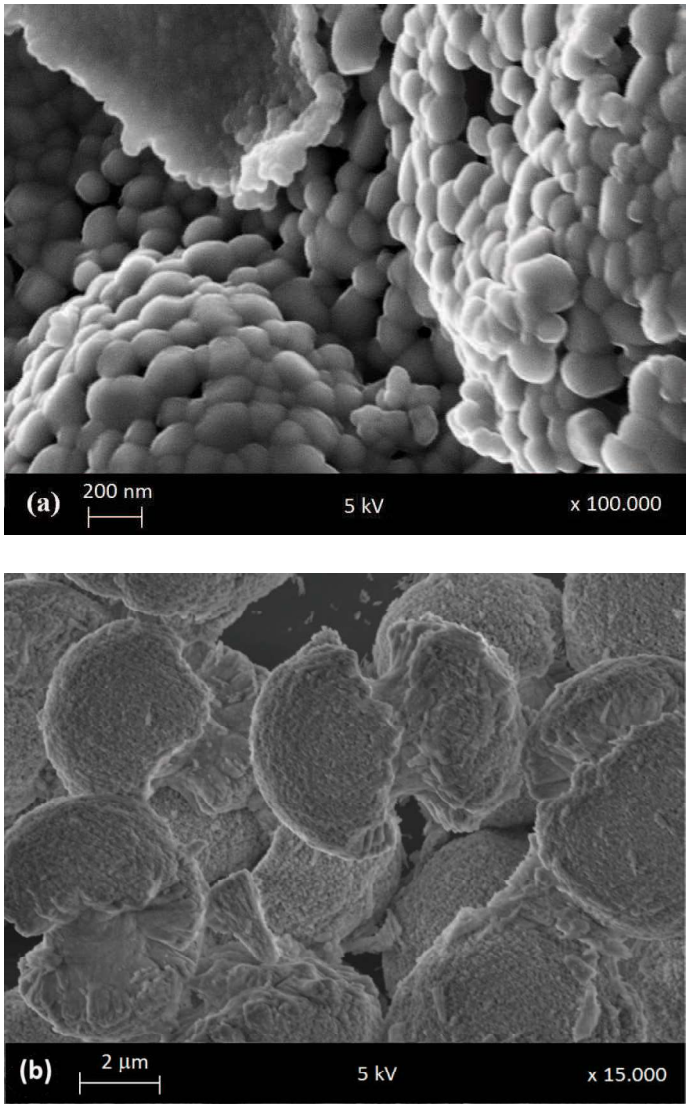

Figure 4.2. FE-SEM images of (a) CWOP and (b) CWOH powders.
Source: By the author.

4.3.3 Nitrogen adsorption–desorption

The N_2 adsorption–desorption isotherms of $CaWO_4$ synthesized by PPM and MAH are shown in Fig. 4.3. The isotherms resemble those of type III isotherms (BDDT classification) and exhibit a H3-type hysteresis loop, which demonstrates some aggregation of plate-like crystals, yielding slit-shaped pores.[35] The Langmuir surface area of obtained samples are about 7 and 12 $m^2.g^{-1}$ for CWOP and CWOH samples, respectively.

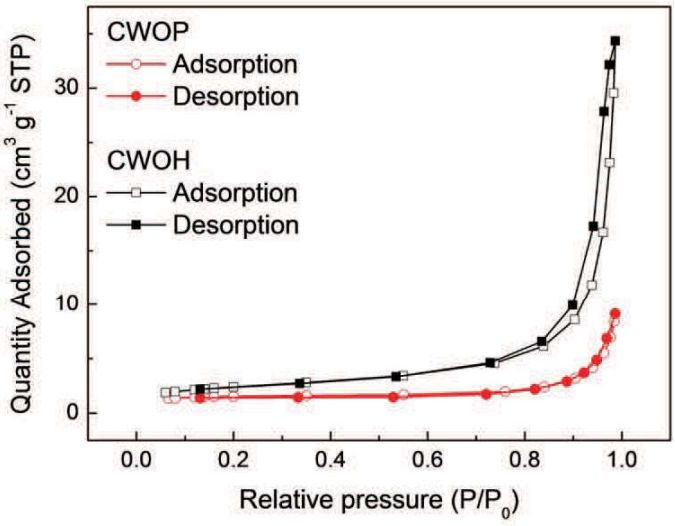

Figure 4.3.The N_2 adsorption–desorption isotherms of $CaWO_4$ synthesized by PPM and MAH.
Source: By the author.

4.3.4 UV-Visible absorption measurements

UV-Vis spectroscopy measurements were performed in the diffuse reflectance mode and the optical band gap energy (Eg) was calculated by the method proposed by Kubelka-Munk for any wavelength.[11,36] The Figure 4.4 shows the Eg obtained and Table 4.2 shows the Eg values obtained in this work and values found in the literature.[11,37-40] Differences of Eg value may be related to particle morphology, type of synthesis, time and temperature of the process. All these factors result in different structural defects, such as oxygen vacancies and link distortions, which are able of promoting the formation of intermediate states of energy within the band gap.[41]

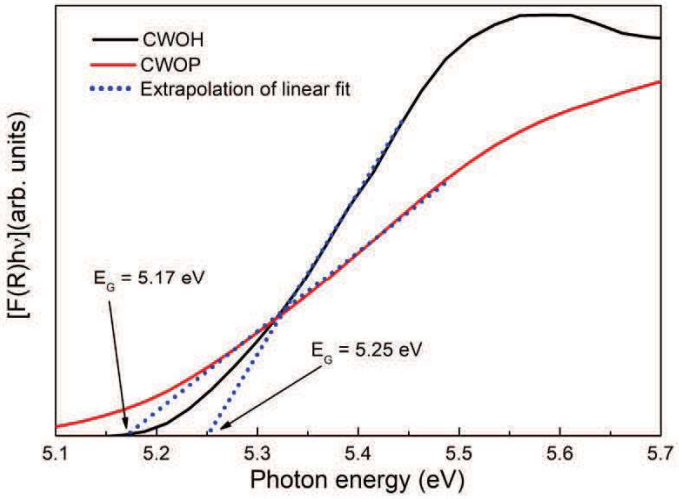

Figure 4.4. Optical band gap energy (E_g) calculated by the method proposed by Kubelka - Munk for any wavelength of $CaWO_4$ powders synthesized by MAH and PPM.
Source: By the author.

Table 4.2. Eg values obtained in this work (*) and values found in the literature. MPP = Polymeric precursor method; MAH = Microwave-assisted hydrothermal; CP = Co-precipitation; SR = Sonochemistry reaction. SPR = Solid-phase reaction.

Method	PPM	HAM	CP	HAM	SR	PPM	SPR
Eg (eV)	5.17	5.23	5.39	5.56	4.08	5.27	4.86
Ref.	*	*	[37]	[11]	[38]	[39]	[40]

Source: By the author.

According to the literature, $CaWO_4$ exhibits an optical absorption spectrum governed by direct electronic transitions and the maximum-energy states in the valence band coincide with the minimum-energy states in the conduction band.[1,42] The valence and conduction bands near the band gap are dominated mainly by contributions from molecular orbitals associated with the WO_4^{-2} ions.[43]

4.3.5 PL measurements

Photoluminescence properties of the $CaWO_4$ (Fig. 4.5) structures were also measured. With excitation wavelength at 350 nm, PL spectra exhibit a broad band covering the visible electromagnetic spectrum in the range of 360 to 750 nm. The profile of the emission band is

characteristic of processes at various levels involving the participation of several states within the band gap.[16] The materials showed green emission peaks of 492 nm e 495 nm for $CaWO_4$ prepared by PPM and MAH, respectively.

In order to evaluate the colorimetric performance of the materials, the emissions colors were analyzed using the Commission Internationale de l'Eclairage (CIE, 1964) chromaticity coordinates x;y. The inset in Figure 4.5 shows the CIE chromaticity diagram for the emission spectra of CWOP and CWOH under 350 nm excitation wavelength. The calculated CIE coordinates for CWOP are x = 0.26, y = 0.50 and for CWOH the coordinates are x = 0.30, y = 0.44. These coordinates are located in the green area at the diagram.

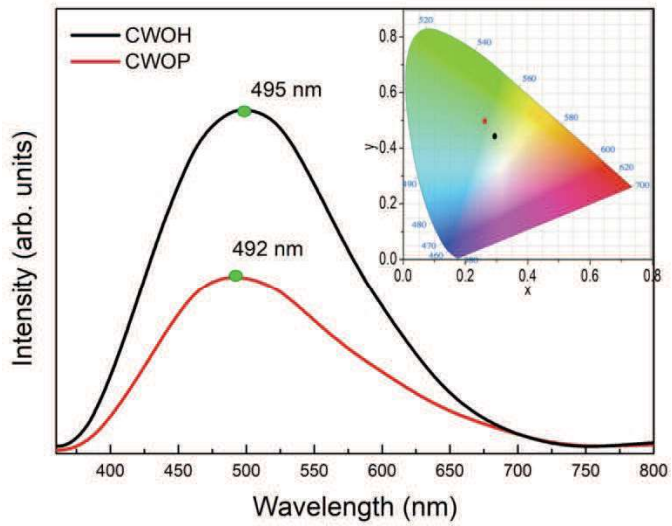

Figure 4.5. PL spectra of $CaWO_4$ powders (λ_{EXC} = 350 nm). The maximum emission peaks are centered on 492 nm and 495 nm for CWOP and CWOH, respectively. Inset: CIE chromaticity diagram for the emission spectra of $CaWO_4$ powders.
Source: By the author.

According to Cavalcante et al.[11] and Campos et al.,[39] the green emission of tungstates have different interpretations. In general, two different mechanisms are responsible for the green emission spectra of $CaWO_4$ crystals: the disorder caused by $[WO_4]^{2-}$ complexes due to the vacancies as $[WO_3 \,.\, V^z_O]$ (where $V^Z_O = V^{\bullet}_O$ or $V^{\bullet\bullet}_O$) and intrinsic slightly distorted $[WO_4]$ tetrahedral in a short range in the ordered structure.[31,39,44]

It is known in the literature that $CaWO_4$ samples with various morphologies exhibit different photoluminescence properties.[30,45] In this work, rounded and dumbbells-like particles showed PL emission peaks position are very near, however the emission intensity was strongly influenced by the temperature of the synthesis. The material prepared by MAH (synthesized at 140 °C) have higher emission intensity when compared to the material synthesized by PPM (synthesized at 700 °C). Moreover, several factors influence the emission intensity such as the degree of aggregation and orientation between the particles, variations in particle size distribution and surface defects.[19]

4.3.6 X-ray absorption spectroscopy measurements

X-ray absorption spectroscopy (XAS) is a powerful tool for the investigation of local structures and provides meaningful additional structural information on materials. Although the local structural data afforded by XAS are usually not sufficient to construct a whole structural model, they often provide valuable information about the local structural peculiarities.

Fig. 4.6 presents the XANES spectra at W L_{III}-edge for $CaWO_4$ samples and a WO_3 standard reference. As it can observed in this figure, XANES spectra for $CaWO_4$ powders exhibit different characteristics compared to the XANES spectrum of the reference compound (WO_3). In these spectra, the white line mainly derives from electron transitions from the $2p$ 3/2 state to a vacant $5d$ state.[12] The difference between sample and reference spectra is expected because W atoms are in an octahedral environment for the WO_3 compound.[12] No significant change is observed in these XANES spectra as a function of the preparation method for $CaWO_4$ samples.

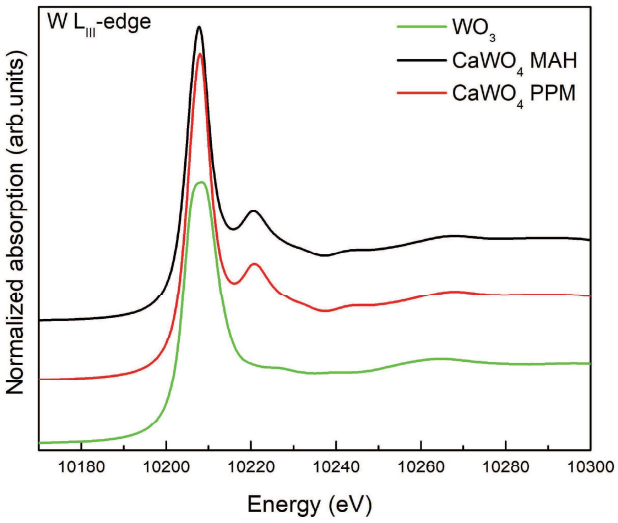

Figure 4.6. XANES spectra at W L_{III}-edge of $CaWO_4$ powders.
Source: By the author.

EXAFS spectra at W L_{III}-edge were also measured in order to obtain quantitative information at local structure such as the number, position and identity of atoms surrounding the absorbing element as well as structural disorder within the coordination spheres.[14] Fig. 4.7 shows the modulus of k^3 weighted Fourier transform of $CaWO_4$ samples extracted from W L_{III}-edge spectra. According to the structural model calculated from the FEFF9 code and crystallographic information according to the XRD measurements, the absorber atom is surrounded by, in this order, two shells with four O atoms each, two shells with four Ca atoms each, one shell with four W atoms and three shells with four O atoms each. Thus, the more intense peak, between 1.0 and 2.0 Å in the Fourier transforms, corresponds to a single scattering interaction between the first four O atoms around the absorber atom. The single scattering interactions relative to W–Ca, W-W and W-O (beyond the first O neighbors) paths correspond the region observed between 2.0 and 5.0 Å. This region also includes multiple scattering.

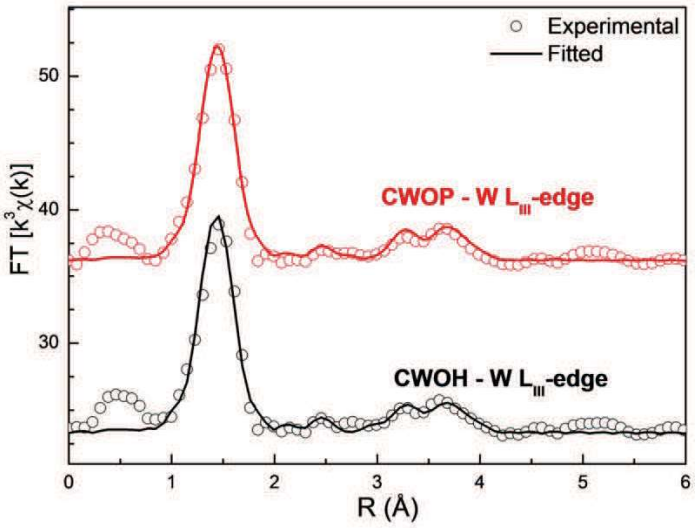

Figure 4.7. Experimental and fitted modulus of k^3 weighted Fourier transform for $CaWO_4$ powders at W L_{III}-edge. Open symbols are experimental data, and solid lines represent fittings using the parameters listed in Table 4.3.
Source: By the author.

Fourier transform curves were then back Fourier transformed between 1.0 and 4.0 Å to obtain the experimental EXAFS spectra to fit using a theoretical model calculated from the FEFF9 code and crystallographic information according the XRD measurements. In all fits, the number of free parameters was kept smaller than the number of independent points, which is defined as $N_{ind} = 2\Delta R\Delta k/\pi$, where ΔR is the width of the R-space filter windows and ΔK is the actual interval of the fit in the k space.[46] The reliability of the fit, determined by a quality factor (Q),[47] the interatomic distances (R) and Debye–Waller factor (σ^2) relatives to the best fits are shown in Table 4.3.

Table 4.3. W L_{III}-edge EXAFS simulation results. R is the distance from the central atom, N is the average coordination number, σ^2 the Debye–Waller factor, and Q the quality factor.

Shell	R (Å)		N		σ^2 (10^{-2} Å^2)		Q	
	MAH	PPM	MAH	PPM	MAH	PPM	MAH	PPM
W-O	1.78(1)	1.78(1)	4.29(16)	4.28(17)	0.082(42)	0.08(2)	2.55	2.13
W-O	2.88(1)	2.89(2)	2.09(41)	2.15(59)				
W-Ca	3.67(1)	3.68(1)	2.34(42)	1.65(65)				
W-Ca	3.84(1)	3.84(1)	0.07(3)	4.31(85)				
W-W	3.90(1)	3.90(1)	2.19(63)	4.93(1.07)	0.74(12)	0.87(10)		
W-O	4.02(2)	4.02(4)	0.005(19)	6.52(1.50)				
W-O	4.02(2)	4.04(4)	3.98(1.25)	0.00(0.94)				
W-O	4.02(2)	4.04(4)	5.29(1.22)	0.00(0.98)				

Source: By the author.

The results of the fits confirm the supposition that synthesis conditions do not introduce high disorders into the structure. The radial distance (R) for all shells does not change considerably as function of the preparation. Moreover, we can trace an increase of oxygen vacancies following the average coordination number (N) for the fourth and fifth O-shells, since sample prepared by PPM shows a lower coordination number in these shells. It can indicate the presence of imperfectness in the crystal lattice. As shown by FE-SEM micrographs, the average particle size is lower for these samples. Due to this, large amount of the atoms should be placed at the boundary of particles resulting in a lower number of neighbors.[48]

4.3.7 H_2-TPR measurements

The H_2-TPR profiles for the materials are shown in the Fig. 4.8 and the reduction peak temperature and corresponding hydrogen consumption are listed in Table 4.4 bellow.

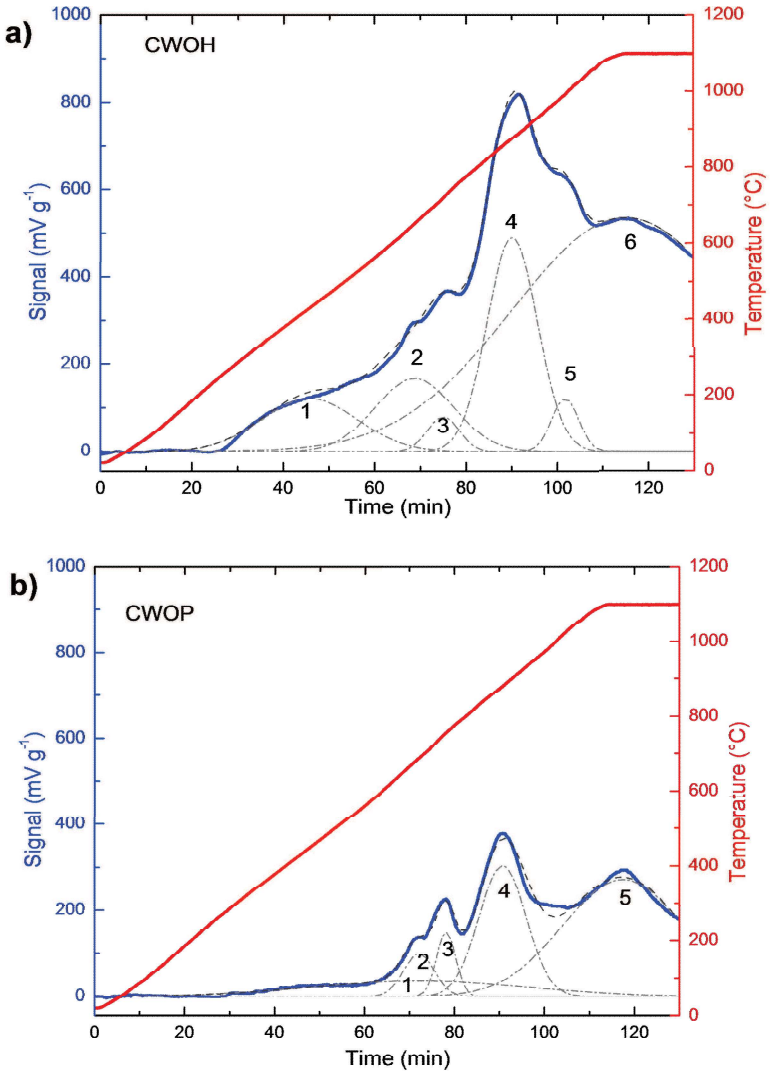

Figure 4.8. H_2-TPR profiles obtained for CWOH (a), and CWOP (b).
Source: By the author.

The $CaWO_4$ samples presented several reduction peaks at the H_2-TPR profiles, with the reduction beginning at about 250 °C for both materials. It can be observed a decreasing of the reduction temperatures for the material produced by MAH method, although the main step reduction still occurs at temperature above 1100 °C for both CWOH e CWOP produced materials. The total hydrogen consumption is larger for the CWOH sample than for CWOP. The CWOH sample shows to possess a high amount of reducible oxide, consuming 2.6 more hydrogen per mass unit than the CWOP one.

Table 4.4. Fit peak data obtained by TPR profiles of the materials produced by both MAH and PPM synthesis methods.

Sample	Peak	Temperature (°C)	Relative Area (%)	H_2 Consumption ($mol.g^{-1}$)	
CWOH	1	429	8	3.54×10^{-4}	4.43×10^{-3}
	2	643	9	3.99×10^{-4}	
	3	715	2	8.86×10^{-5}	
	4	873	17	7.53×10^{-4}	
	5	988	2	8.86×10^{-5}	
	6	1100	62	2.75×10^{-3}	
CWOP	1	685	14	2.51×10^{-4}	1.79×10^{-3}
	2	689	6	1.07×10^{-4}	
	3	753	5	8.95×10^{-5}	
	4	879	26	4.65×10^{-4}	
	5	1100	49	8.77×10^{-4}	

Source: By the author.

4.3.8 Catalytic activity toward toluene oxidation

Gas-phase toluene oxidation was selected as a probing reaction to evaluate the catalytic potential of the $CaWO_4$ prepared samples. The results are presented in Fig. 4.9.

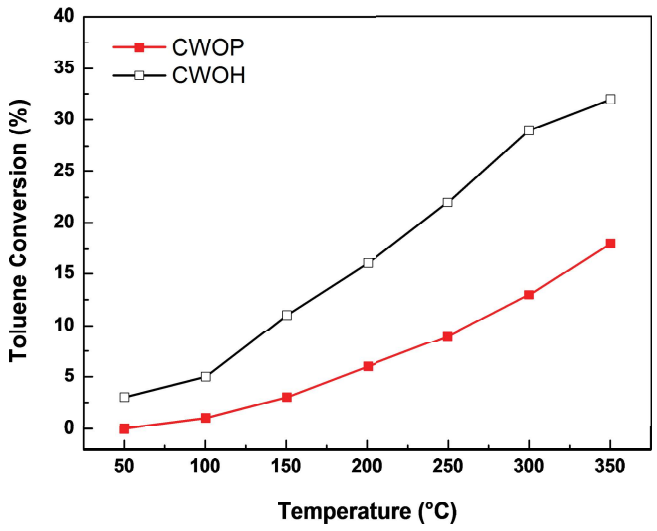

Figure 4.9. Gas-phase toluene conversion over $CaWO_4$ catalysts as a function of reaction temperature.
Source: By the author.

Previously, the toluene thermal oxidation was carried out without the catalyst. Toluene conversion was negligible at low temperatures. The process started at 350 °C achieving only about 3% of conversion at 500 °C (not shown). In the presence of the catalyst, no significant toluene conversion could be observed at very low temperatures (below 100 °C). The catalysts displayed appreciable activities from 150 °C, particularly CWOH that reached almost 11% of toluene conversion. The catalysts showed a similar tendency, that is, an increase in the toluene conversion with the increase in the reaction temperature. However, it can be easily seen that CWOH showed greater catalytic activity than CWOP. For example, 10% of toluene conversion was achieved at about 140 °C over CWOH, whereas the same conversion required approximately 260 °C over CWOP. Comparing the specific surface areas of both catalysts, it could be conclude that this property had only a minor influence on the catalytic activities presented, since the specific surface areas were similar. The superior performance of CWOH catalyst can be ascribed to its higher reducibility and oxygen mobility, estimated by means of H_2-TPR measurements, as it can be deduced from Fig. 4.8 and Table 4.4. The catalyst reducibility can be related to the position, shape and intensity of the reduction peaks of H_2-TPR curves.[49] The reduction peaks for each sample (Fig. 4.8) presented such differences which indicate that the catalyst reducibility is affected by the preparation method. Intense reduction peaks as well as the shifting of reduction peaks to lower temperatures were observed in the H_2-TPR profile of CWOH sample, indicating that this catalyst can be more reducible than CWOP one. Besides, the surface oxygen mobility increase can be associated with the decrease in the temperature at which the reduction peak appears. Mobile surface oxygen species can be easily removed under reduction atmosphere and higher mobility of surface these ions helps in the removal of lattice oxygen during the reduction process.[50] This phenomenon could indicate that the amount of this element at the surface increases due to the diffusion of bulk oxygen to the surface. Thus, more bulk oxygen can be reduced resulting in

more lattice oxygen involved in the oxidation for CWOH catalyst.[49-52] According to Sun et al.,[53] the higher reducibility means the higher mobility of these species in a catalyst. So, in this case, CWOH sample has the highest oxygen mobility. In addition, from Table 4.4, the consumption amount of hydrogen varies from 4.43 x 10^{-3} mol.gcat^{-1} for CWOH, which was the most active, to 1.79 x 10^{-3} mol.gcat^{-1} for CWOP, which was the less active catalyst. This result also indicates that the mobile oxygen species available on the CWOH surface are larger than that of CWOP.[54] The bulk and surface oxygen mobility play an important role in hydrocarbon oxidation reactions, in which the oxidation-reduction cycles determine the activity of the material. The higher oxygen mobility facilitates the migration of oxygen species (that are consumed to oxidize toluene) across the catalyst structure, resulting in higher oxidation activity. Previous studies have demonstrated that toluene oxidation promoted by metal oxide catalysts follows the Mars-van Krevelen mechanism, in which the key steps are the supply of oxygen by the oxide, the introduction of the oxygen species from the lattice oxide into the substrate molecule and the re-oxidation of the reduced solid by the oxygen-containing gaseous phase, the rate-determining step of the reaction.[51,55-58] Thus, abundant mobility of active lattice oxygen species improves the catalytic activity in the toluene oxidation. Toluene oxidation promoted by $BaWO_4$ and $BaMoO_4$ catalysts was described in our previous paper in which we considered the role of oxygen mobility and oxygen vacancies in the process.[14] In the occasion, the H_2-TPR, O_2-chemisorption and EXAFS results indicated that $BaWO_4$ catalysts, compared with $BaMoO_4$ catalysts, had higher oxygen mobility and oxygen vacancies that appear to be the key factors for the achievement of better catalytic performances.

4.4 Conclusions

$CaWO_4$ polycrystalline powders have been successfully synthesized by microwave-assisted hydrothermal method and by polymeric precursor method with scheelite-type tetragonal structure without secondary phase. Obtained particles have rounded and dumbbell-like morphology based on surfactant and polymeric agents under different experimental conditions. N_2 adsorption-desorption isotherms are of type III and exhibit a H3-type hysteresis loop. The optical band gap energy was calculated by the method proposed by Kubelka- Munk and the values obtained were about 5.2 eV. The PL emissions of these tungstates samples mainly attribute to the charge transfer within the $[WO_4]$ tetrahedron complex. Besides that, the powders prepared by MAH showed a higher PL emission intensity than powders prepared by PPM. The H_2-TPR results indicated that $CaWO_4$ sample prepared by MAH, compared with $CaWO_4$ sample prepared by PPM, have higher oxygen mobility that appear to be a key factor for the achievement of better catalytic performances.

ACKNOWLEDGMENTS

The authors gratefully acknowledge the financial support of the Brazilian research funding agencies FAPESP: 2013/07909-4 and 2013/07296-2, CAPES and CNPq. The research was partially carried out at LNLS National Laboratory of Synchrotron Light (proposal number XAFS1 - 19058), Brazil.

4.5 References

1 ZHANG, Y.; HOLZWARTH, N. A. W.; WILLIAMS, R. T. Electronic band structures of the scheelite materials $CaMoO_4$, $CaWO_4$, $PbMoO_4$ and $PbWO_4$. **Physical Review B**, v. 57, n. 20, p. 12738-12750, 1998.

2 GILLETTE, R. H. Calcium and cadmium tungstate as scintillation counter crystals for gamma-ray detection. **Review Scientific Instruments**, v. 21, p .294-301, 1950. doi:10.1063/1.1745567.

3 OISHI, S.; HIRAO, M. Growth of $CaWO_4$ whiskers from KCl flux. **Journal of Materials Science Letters**, v. 8, p. 1397-1398, 1989.

4 NAGIRNYI, V. et al. Excitonic and recombination processes in $CaWO_4$ and $CdWO_4$ scintillators under synchrotron irradiation. **Radiation Measurements**, v. 29, p. 247-250, 1998. doi:10.1016/S1350-4487(98)00017-1.

5 XIANG, Y. et al. Synthesis of $CaMoO_4$ hierarchical structures via a simple slow-release co-precipitation method. **Applied Surface Science**, v. 349, p. 374-379, 2015. doi:10.1016/j.apsusc.2015.04.228.

6 BOURAJOINI, H. et al. Calcium Manganese oxide catalysts for water oxidation: Unravelling the influence of various synthesis strategies. **Materials Research Bulletin**, v. 79, p. 133-137, 2016. doi:10.1016/j.materresbull.2016.03.018.

7 WATCHARATHAMRONGKUL, K. et al. Calcium oxide based catalysts for ethanolysis of soybean oil. **Songklanakarin Journal Science and Technology,** v. 32, n. 6, p. 627-634, 2010.

8 AVRAMOVIĆ, J. M. et al. Optimization of sunflower oil ethanolysis catalyzed by calcium oxide: RSM versus ANN-GA. **Energy Conversion and Management,** v. 105, p. 1149-1156, 2015. doi:10.1016/j.enconman.2015.08.072.

9 LANG, R. J.; NEAVEL, R. C. Behaviour of calcium as steam gasification catalyst. **Fuel**, v. 61, p. 620-626, 1982.

10 LECEA, C. S. M.; ALARCÓN, M. A.; SOLANO, A. L. Calcium-catalysed carbon gasification in CO_2 and steam. **Fuel**, v. 69, p. 21-27, 1990.

11 CAVALCANTE, L. S. et al. Electronic structure, growth mechanism and photoluminescence of $CaWO_4$ crystals. **Crystal Engineering Communications**, v. 14, p. 853-868, 2012. doi:10.1039/c1ce05977g.

12 GRACIA, L. et al. Presence of excited electronic state in $CaWO_4$ crystals provoked by tetrahedral distortion: An experimental and theoretical investigation. **Journal of Applied Physics**, v. 110, p. 043501 (11), 2011. doi:10.1063/1.3615948.

13 YU, P. et al. Preparation and microstructure of $CaMoO_4$ ceramic films prepared through electrochemical technique. **Journal of Electroceramics**, v. 16, p. 473-476, 2006. doi:10.1007/s10832-006-9900-6.

14 ALENCAR, L. D. S. et al. Preparation, characterization and catalytic application of Barium molybdate ($BaMoO_4$) and Barium tungstate ($BaWO_4$) in the gas-phase oxidation of toluene. **Ceramics International**, v. 43, n. 5, p. 4462–4469, 2017. doi:10.1016/j.ceramint.2016.12.096.

15 MAURERA, M. A. M. A. et al. Microstructural and optical characterization of $CaWO_4$ and $SrWO_4$ thin films prepared by a chemical solution method. **Materials Letters**, v. 58, p. 727-732, 2004. doi:10.1016/j.matlet.2003.07.002.

16 WILSON, G. J. et al. Modification of TiO_2 for enhanced surface properties: finite Ostwald ripening by a microwave hydrothermal process. **Langmuir**, v. 22, p. 2016-2027, 2006. doi:10.1021/la052716j.

17 HUANG, H. et al. Low temperature catalytic oxidation of volatile organic compounds: a review. **Catalysis Science and Technology**, v. 5, p. 2649-2669, 2015. doi:10.1039/C4CY01733A.

18 BILECKA, I.; NIEDERBERGER, M. Microwave chemistry for inorganic nanomaterials synthesis. **Nanoscale**, v. 2, p. 1358-1374, 2010. doi:10.1039/b9nr00377k.

19 LI, W. B.; WANG, J. X.; GONG, H. Catalytic combustion of VOCs on non-noble metal catalysts. **Catalysis Today,** v. 148, p. 81-87, 2009. doi:10.1016/j.cattod.2009.03.007.

20 LIOTTA, L. F. Catalytic oxidation of volatile organic compounds on supported noble metals. **Applied Catalysis B:Environmental,** v. 100, p. 403-412, 2010. doi:10.1016/j.apcatb.2010.08.023.

21 KAMAL, M. S.; RAZZAK, S. A.; HOSSAIN, M. M. Catalytic oxidation of volatile organic compounds (VOCs) – A review. **Atmospheric Environment**, v. 140, p. 117-134, 2016. doi:10.1016/j.atmosenv.2016.05.031.

22 MICHALOWICZ, A. et al. MAX: Multiplatform applications for XAFS. **Journal of Physics: Conference Series**, v. 190, p. 012034 (4), 2009. doi:10.1088/1742-6596/190/1/012034.

23 ANKUDINOV, A. L. et al. Real-space multiple-scattering calculation and interpretation of x-ray-absorption near-edge structure. **Physical Review B**, v. 58, n. 12, p. 7565-7576, 1998. doi:10.1103/PhysRevB.58.7565.

24 CULLITY, D. B., **Elements of X-ray Diffraction**, Addison-Wesley Inc., Massachusetts; 1956.

25 THONGTEM, T. et al. Luminescence and absorbance of highly crystalline $CaMoO_4$, $SrMoO_4$, $CaWO_4$ and $SrWO_4$ nanoparticles synthesized by co-precipitation method at room temperature. **Journal of Alloys and Compounds**, v. 506, p. 475-481, 2010. doi:10.1016/j.jallcom.2010.07.033.

26 YANG, Y.; WANG, X.; LIU, B. Synthesis of $CaWO_4$ and $CaWO_4$:Eu microspheres by precipitation. **Nano**, v. 9, p. 1450008(6), 2014. doi:10.1142/S1793292014500088.

27 SU, Y. et al. Tunable physical properties of $CaWO_4$ nanocrystals via particle size control. **Journal of Physical Chemistry C**, v. 111, p. 6684-6689, 2007. doi:10.1021/jp068480p.

28 SEN, A.; PRAMANIK, P. A chemical synthetic route for the preparation of fine-grained metal tungstate powders (M = Ca, Co, Ni, Cu, Zn). **Journal of the European Ceramic Society**, v. 21, p. 745-750, 2001.

29 RYU, J. H. et al. Microwave-assisted synthesis of nanocrystalline MWO_4 (M: Ca, Ni) via water-based citrate complex precursor. **Ceramics International**, v. 31, p. 883-888, 2005. doi:10.1016/j.ceramint.2004.09.015.

30 CHEN, Z. et al. Controllable synthesis of hierarchical nanostructures of $CaWO_4$ and $SrWO_4$ via facile low-temperature route. **Materials Research Bulletin**, v. 44, p. 45-50, 2009. doi:10.1016/j.materresbull.2008.04.008.

31 THONGTEM, T.; PHURUANGRAT, A; THONGTEM, S. Synthesis of $CaWO_4$, $SrWO_4$ and $BaWO_4$ with nanosized particles using cyclic microwave radiation. **Journal of Ceramic Processing Research**, v. 9, n. 3, p. 258-261, 2008.

32 WANG, G.; LIN, S.; WAN, G. Growth process and optical properties of $SrWO_4$ microcrystal prepared by a microwave-assisted method. **Synthesis and Reactivity in Inorganic, Metal-Organic, and Nano-Metal Chemistry**, v. 42, p. 888-891, 2012. doi:10.1080/15533174.2011.652283.

33 ZHANG, L. et al. Dumbbell-like $BaWO_4$ microstructures: surfactant-free hydrothermal synthesis, growth mechanism and photoluminescence property. **Superlattices and Microstructures**, v. 54, p. 87-95, 2013. doi:10.1016/j.spmi.2012.11.010.

34 LI, Y. F. at al. Room-temperature template-free synthesis of dumbbell-like $SrSO_4$ with hierarchical architecture. **Journal of Crystal Growth**, v. 312, p. 1886-1890, 2010. doi:10.1016/j.jcrysgro.2010.03.007.

35 GREGG, S.J.; SING, K. S. W. **Adsorption, Surface Area and Porosity**. Academic Press, London, 1967.

36 MORALES, A. E.; MORA, E. S.; PAL, U. Use of diffuse reflectance spectroscopy for optical characterization of un-supported nanostructures. **Revista Mexicana de Física**, v. 53, n. 5, p. 18-22, 2007.

37 VIEIRA, E. G. et al. Síntese pelo método da coprecipitação e caracterização estrutural do tungstato de cálcio com estrutura tipo scheelita. **Cerâmica**, v. 59, p. 417-425, 2013. doi:10.1590/S0366-69132013000300011.

38 GHOREISHI, S. M. Facile synthesis and characterization of $CaWO_4$ nanoparticles using a new Schiff base as capping agent: enhanced photocatalytic degradation of methyl orange. **Journal of Materials Science: Materials in Electronics**, v. 28, p. 14833-14838, 2017. doi:10.1007/s10854-01707354-z.

39 CAMPOS, A. B. et al. Mechanisms behind blue, green, and red photoluminesce emissions in $CaWO_4$ and $CaMoO_4$ powders. **Applied Physics Letters**, v. 91, p. 051923 (3), 2007. doi:10.1063/1.2766856.

40 BAKOVETS, V. V. et al. Bandgap-width correction for luminophores $CaMoO_4$ and $CaWO_4$. **Optics and Spectroscopy**, v. 3, n. 3, p. 399-403, 2017. doi:10.1134/S0030400X17090053.

41 LONGO, V. M. et al. Hierarchical assembly of $CaMoO_4$ nano-octahedrons and their photoluminescence properties. **Journal of Physical Chemistry C**, v. 115, p. 5207-5219, 2011. doi:10.1021/jp1082328.

42 PERALES, R. L. et al. Optical absorption of divalent metal tungstates: Correlation between the band-gap energy and the cation ionic radius. **Europhysics Letters**, v. 83, p. 37002 (5), 2008. doi:10.1209/0295-5075/83/37002.

43 TABLERO, C. Optical absorption and applications of the ABO_4 (A = Ca, Pb and B = Mo, W) semiconductors. **Chemical Physics Letters**, v. 635:, p. 190-195, 2015. doi:10.1016/j.cplett.2015.06.074.

44 MARQUES, V. S. et al. Effect of different solvent ratios (water/ethylene glycol) on the growth process of $CaMoO_4$ Crystals and their optical properties. **Crystal Growth & Design**, v. 10, p. 4752-4768, 2010. doi:10.1021/cg100584b.

45 ZHANG, Y. et al. Controllable synthesis and luminescent properties of hierarchical flowerlike $CaMoO_4$ microspheres. **Nano-Structures and Nano-Objects**, v. 6, p. 46-51, 2016. doi:10.1016/j.nanoso.2016.03.008.

46 ROCCA, F. et al. XANES and EXAFS at Mo K-edge in $(AgI)_{1-x}(AgMoO_4)_x$ glasses and crystals. **Solid State Ionics**, v. 121, p. 189-192, 1999.

47 HASNAIN, S. S. Report on the International Workshops on Standards and Criteria in XAFS. **X-ray Absorption Fine Structure**: Proceedings of the VI International Conference on X-ray Absorption Fine Structures, Ellis Horwood, New York, 1991.

48 CURCIO, A. L.; BERNARDI, M. I. B.; Mesquita, A. Local Structure and photoluminescence properties of nanostructured $Zn_{1-x}Mn_xS$ Material. **Physica Status Solidi C**, v. 12, n. 12, p. 1367-1371, 2015. doi:10.1002/pssc.201510135.

49 SILVA, A. G. M. et al. $Ce_{1-x}Sm_xO_{1.9-\delta}$ nanoparticles obtained by microwave-assisted hydrothermal processing: an efficient application for catalytic oxidation of α-bisabolol. **Catalysis Science and Technology**, v. 4, p. 814-821, 2014. doi:10.1039/c3cy00788j.

50 RAO, G. R.; MISHRA, B. G. Structural, redox and catalytic chemistry of ceria based materials. **Bulletin of the Catalysis Society of India**, v. 2, p. 122-134, 2003.

51 LIU, P. et al. An efficient catalyst of manganese supported on diatomite for toluene oxidation: Manganese species, catalytic performance, and structure-activity relationship. **Microporous and Mesoporous Materials**, v. 239, p. 101-110, 2017. doi:10.1016/j.micromeso.2016.09.053.

52 SIHAIB Z. et al. Manganese oxide-based catalysts for toluene oxidation, **Applied Catalalysis B: Environmental**, v. 209, p. 689-700, 2017. doi:10.1016/j.apcatb.2017.03.042.

53 SUN M. et al. Manganese oxides with different crystalline structures: Facile hydrothermal synthesis and catalytic activities. **Materials Letters**, v. 86, p. 18-20, 2012. doi:10.1016/j.matlet.2012.07.011.

54 SUN, G. B. et al. A crucial role of surface oxygen mobility on nanocrystalline Y_2O_3 support for oxidative steam reforming of ethanol to hydrogen over Ni/Y_2O_3 catalysts. **Applied Catalysis B: Environmental**, v. 81, p. 303-312, 2008. doi:10.1016/j.apcatb.2007.12.021.

55 DOORNKAMP C.; PONEC, V. The universal character of the Mars and Van Krevelen mechanism. **Journal of Molecular Catalysis A: Chemical**, v. 162, p. 19-32, 2000. doi:10.1016/S1381-1169(00)00319-8.

56 QU, Z. et al. The improved reactivity of manganese catalysts by Ag in catalytic oxidation of toluene. **Applied Catalysis B: Environmental**, v. 132-133, p. 353–362, 2013. doi:10.1016/j.apcatb.2012.12.008.

57 LIU, Y. et al. Mesoporous Co_3O_4-supported gold nanocatalysts: Highly active for the oxidation of carbon monoxide, benzene, toluene, and o-xylene. **Journal of Catalysis**, v. 309, p. 408-418, 2014. doi:10.1016/j.jcat.2013.10.019.

58 GÓMEZ, D.M. et al. TAP study of toluene total oxidation over Co_3O_4/La-CeO_2 catalyst with an application as a washcoat of cordierite honeycomb monoliths. **Physical Chemistry Chemical Physics**, v. 16, p. 11447-11455, 2014. doi:10.1039/C4CP00886C.

5 PAPER 3.

Short- and long-range structural characterization of $CaMoO_4$ powders prepared by microwave assisted hydrothermal and polymeric precursor methods

Lorena D. S. Alencar*[1,2], Alexandre Mesquita[3], Maria I. B. Bernardi[1]

[1.] Instituto de Física de São Carlos, Universidade de São Paulo, USP, 13563-120, São Carlos, SP, Brazil.

[2.] Instituto Federal de Mato Grosso do Sul, IFMS, 79310-110, Corumbá, MS, Brazil.

[3.] Instituto de Geociências e Ciências Exatas, Unesp, Universidade Estadual Paulista, Departamento de Física, 13506-900, Rio Claro, SP, Brazil.

*Corresponding authors. Tel: +55 16 3373 9828. E-mail address : lorena.alencar@ifms.edu.br

Abstract: Calcium molybdate ($CaMoO_4$) has been extensively studied due to its excellent optical properties, as well as thermal stability and efficient absorption of high energy radiation. Several processes have been used to synthesize successfully $CaMoO_4$ powders. Among them, the microwave assisted hydrothermal (MAH) and polymeric precursor methods (PPM) are considered excellent strategies for the preparation of this material because of the possible morphological and compositional homogeneities. However, to the best of our knowledge, there are no structural characterizations of $CaMoO_4$ at local-range by X-ray absorption spectroscopy (XAS) in the literature. In this paper, $CaMoO_4$ powders were obtained by MAH and PPM methods, forming a single scheelite-type tetragonal structure phase. Scanning electron microscopy images reveal agglomerated rounded morphology in which particles present an average diameter of nearly 100 nm and particles in clusters dumbbells-like shaped for PPM and MAH methods, respectively. Micro-Raman spectra show that both methods produce $CaMoO_4$ without structural alterations, presenting only different morphologies. The X-ray absorption near edge structure (XANES) and extended X-ray absorption fine structure (EXAFS) results of the fits confirm that preparation method does not introduce high order disorders into the structure.

Keywords: $CaMoO_4$, XAS, XANES, EXAFS, Raman, microwave assisted hydrothermal, polymeric precursor method

5.1 Introduction

Calcium molybdates ($CaMoO_4$), pure and doped, have been studied for eight decades by several researchers.[1] All this attention to this compound can be justified by its excellent optical properties, as well as thermal stability and efficient absorption of high energy radiation,[2] which can be used in LEDs, fluorescent light bulbs,[3] the production of white light emitting diode,[2] applications as solid state laser,[4] scintillators,[5] in heterogeneous photocatalytic processes for dye photodegradation,[6] among other applications.

The $CaMoO_4$ belongs to the scheelite family with body-centered tetragonal structure and space group ($I4_1/a$) with symmetry C^6_{4h}. In its structure, the network-modifying cations (calcium) are coordinated to eight oxygen atoms forming a cluster with dodecahedron configuration [CaO_8] and the network-forming cations (molybdenum) are coordinated to four oxygen atoms forming a cluster of [MoO_4] with a tetrahedral configuration.[7,8]

The literature reports several methods of obtaining $CaMoO_4$ whose preparation procedures are able to modify the morphology, particle size distribution, crystallographic orientation and lattice defects which transform structural, electrical, optical or catalytic properties, study can lead to a better understanding and influencing on technological application of this material.[2,9] Therefore, over the years the methods have been improved to obtain $CaMoO_4$ crystals, such as vapor diffusion sol-gel,[7] co-precipitation method,[10] conventional hydrothermal,[11] microwave assisted hydrothermal system (MAH)[12] and the polymeric precursor method (PPM).[13] The last two methods, MAH and PPM, were chosen in order to prepare $CaMoO_4$ powders in this study. MAH is efficient because it presents a shorter synthesis time and allows greater organization of the crystalline structure at low synthesis temperature[14] and PPM is an effective soft chemical method that promotes morphological and compositional homogeneities at the prepared complex oxide material, reducing segregation of

the metals, ensuring compositional homogeneity on the molecular scale by immobilizing the metal complex in rigid organic polymeric networks.[14]

Despite all the studies dedicated to this composition, the short and long-range order structure of the $CaMoO_4$ system evaluated using X-ray absorption spectroscopy (XAS) has not been found in the literature. XAS has been an important characterization technique to describe the local and medium-range atomic structure. This technique provides information on the electronic and structural properties around the absorber element choosing the proper absorption edge, which enable the use of this tool in several systems in amorphous and crystalline solids, dispersed systems and thin films.[15] Thus, this work aimed to obtain $CaMoO_4$ powders by the two methods mentioned above and to characterize the local and electronic structure in order to verify the effect of the preparation method on local structure of this material.

5.2 Experimental

5.2.1. Samples preparation

$CaMoO_4$ powders obtained by MAH ($CaMoO_4$ MAH): 5 x 10^{-3} mol of CaN_2O_6-$4H_2O$ (Sigma-Aldrich, 99%) and $MoNa_2O_4$-$2H_2O$ (Sigma-Aldrich, 99.5%)were added with ethylene glycol (EG) (Synth, 99%) in distilled water at 70 °C. The H_2O:EG ratio is 5.3. It was add NH_4OH (Synth, 27%) to adjusted the pH to 11 in order to increase the hydrolysis rate, leading to precipitate formation. This solution was transferred to a Teflon cup and then for into the autoclave coupled to a domestic microwave oven (2.45 GHz, maximum power of 800 W). The solution was processed at 140 °C for 30 min and the heating rate was set at 25 °C.min^{-1}. After processing, the system was naturally cooled to room temperature and the precipitate was washed several times with distilled water, it was centrifuged and then dried around 80 °C in an oven for about 8 hours to get a white powder.

Synthesis of $CaMoO_4$ powders by polymeric precursor method ($CaMoO_4$ PPM): To obtain CaMoO4 powders by PPM, firstly the molybdenum citrate was obtained by the dissolution of 5.0 x 10^{-2} mol of MoO_3 (Merck, 99.5%) in 100 mL of distilled water under constant stirring and heating of approximately 70 °C mixed into a solution of $C_6H_8O_7$ (Synth, 99.5%) dissolved in 100 mL of distilled water under the same conditions of temperature and stirring. After homogenization, 3.5 x 10^{-2} mol of $Ca(NO_3)_2 – 4H_2O$ (Sigma-Aldrich, 99%) was diluted in 100 mL of distilled water and added to the molybdenum citrate. It was necessary to adjust the pH to between 2 and 3 with HNO_3 (Synth, 65%) to ensure dissolution of MoO_3. EG was added to promote polyesterification of the complex. The citric acid/EG mass proportion is 60:40. The molar ratio between metal cations was 1:1 and the stoichiometry between citric acid/metal was 3:1. The temperature was increased to range of 150 to 200 °C to occur the polyesterification reaction and evaporation of the excess water, obtaining clear and homogeneous resin. The polymer resin was pyrolyzed at 300 °C for 4 hours at a heating rate of 10 °C.min^{-1} in ambient atmosphere. The material obtained was deagglomerated using an agate mortar. These powders were annealed at 700 °C for 2 hours, at a heating rate of 10 °C.min^{-1} in ambient atmosphere.

5.2.2. Samples characterizations

The crystalline phase of the powders was determined by X-ray diffraction (XRD) using a RIGAKU - ULTIMA IV X-Ray diffractometer with Cu-Kα (λ = 1.5406 Å) radiation for 2θ values from 20° to 80°. The morphology was analyzed by scanning electron microscope (SEM; Zeiss – Sigma). The micro-Raman spectra were obtained on a JOBIN-YVON equipment (model T-64000), with a triple monochromator connected to a Charge-Coupled Device (CCD). An argon laser with an excitation line of 514.5 nm and nominal power of 15 mW was used. An objective lens microscope was used to direct the laser

beam. Spectra were recorded over the range 100 – 1000 cm^{-1}. X-ray absorption near edge spectroscopy (XANES) and extended X-ray absorption fine structure (EXAFS) measurements at the Mo K-edges (20000 eV) of $CaMoO_4$ samples were collected in transmission mode as a function of the temperature using a Si(111) channel-cut monochromator at the LNLS (National Synchrotron Light Laboratory) facility using the D04B-XAFS1 beam line. The extraction and fit of the EXAFS spectra were performed using the multi-platform applications for X-ray absorption (MAX) software package[16] and theoretical spectra were obtained using the FEFF9 code.[17]

5.3 Results and discussion

5.3.1 X-ray diffraction analysis

The XRD patterns show that the samples obtained by MAH and PPM crystallize completely without the presence of secondary phases. All the diffraction peaks in Figure 5.1 correspond to $CaMoO_4$ compound in tetragonal scheelite structure (space group $I4_1/a$). According to Inorganic Crystal Structure Database (ICSD) card N° 62219, the cell parameters are $a = b = 5.223$ Å and c = 11.429 Å. These results confirm that the two methods are effective procedures to prepare high-ordered $CaMoO_4$ without spurious phase.

The XRD patterns can also be used to identify average sizes of crystallites (D) by applying the Debye–Scherrer formula, $D = K\lambda/(\beta\cos\theta)$, where K is a constant taken as 0.9, λ is the wavelength of the X-ray radiation ($\lambda = 1{,}54$ Å), β is the full width at half-maximum (FWHM) in radian of the main peak, and θ is the diffracting angle.[18] The crystallite sizes are estimated at 67 and 49 nm for $CaMoO_4$ PPM and $CaMoO_4$ MAH, respectively.

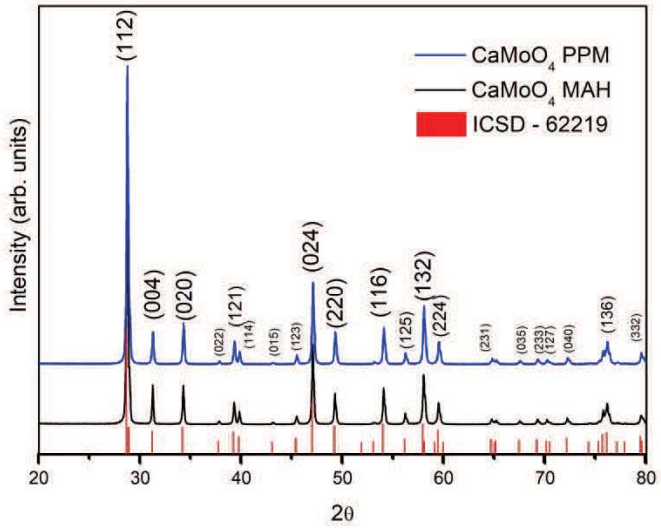

Figure 5.1. XRD patterns of $CaMoO_4$ powders obtained by MAH and PPM.
Source: By the author.

5.3.2 Scanning electron microscope analysis

The $CaMoO_4$ PPM powders exhibits an agglomerated rounded morphology (Fig. 5.2a) in which particles present an average diameter of nearly 100 nm. On the other hand, $CaMoO_4$ MAH powders (Fig. 5.2b) have particles in clusters dumbbells-like shaped. The formation of these clusters with recognizable boundaries was reported earlier in studies concerning tungstates like $SrWO_4$, $CaWO_4$ and $BaWO_4$[19-21] and also for calcium molybdates.[9,22] The possible formation mechanism of these clusters would be the connection of highly oriented nanoparticles with each other during the self-assembly process,[23] which has been proposed by some researchers based on surfactant and polymeric agents under different experimental conditions.[24]

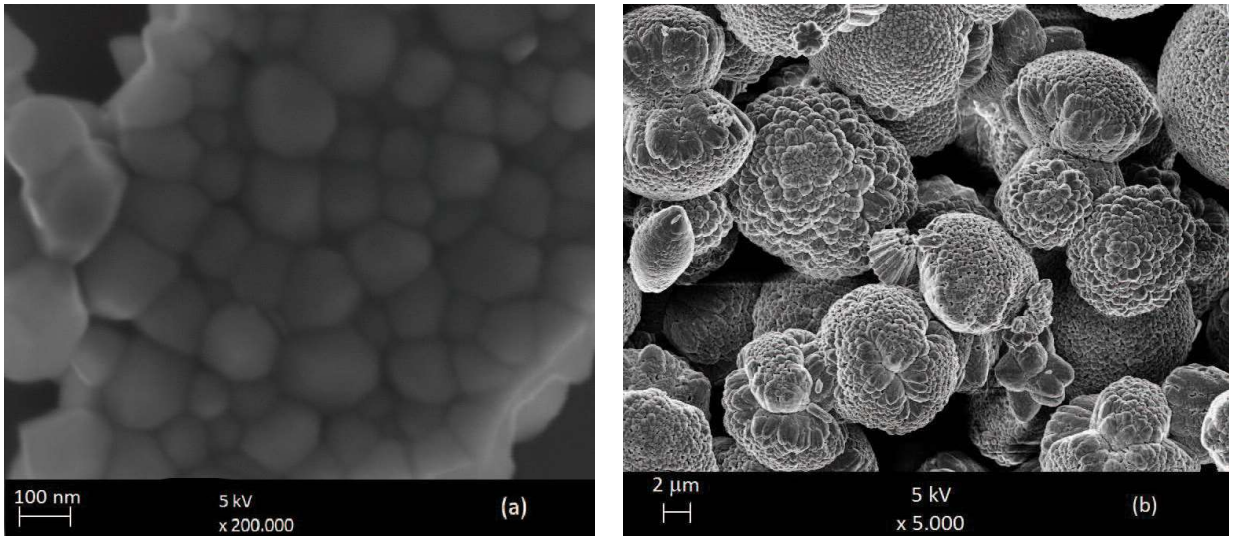

Figure 5.2. FEG-SEM images of (a) $CaMoO_4$ powders prepared by the PPM and (b) $CaMoO_4$ powders prepared by MAH method.
Source: By the author.

5.3.3 Micro-Raman spectroscopy

Micro-Raman spectroscopy is a technique that is based on the inelastic scattering of light by molecules. As a result of this physical phenomenon, there is a change between the frequencies of scattered and incident light that allows the identification of molecular structures by their vibrational modes. For $CaMoO_4$ crystals, prepared by both methods, the calculations of the group theory suggest the presence of 26 different vibrations modes that are represented by Equation 5.1:[25,26]

$$\Gamma = 3A_g + 5A_u + 5B_g + 3B_u + 5E_g + 5E_u \qquad (5.1)$$

The symbols A_g, B_g and E_g represent vibrational active modes in Raman, where A and B are non-degenerate modes while the E modes are doubly degenerated. The subscripts "g" and "u" indicate symmetry operations related to the inversion of the center-symmetrical of the crystal. The Au and Eu modes correspond to frequency zero of acoustic modes, while the Bu modes are optical modes. The A_g, B_g and E_g modes are related to vibration movements within the crystals. Therefore, thirteen active modes are expected in the Raman scattering spectrum for the crystals, represented by Equation 5.2.[27,28]

$$\Gamma = 3A_g + 5B_g + 5E_g \qquad (5.2)$$

Due to the existence of vibrations with very close energies, the overlapping of peaks in the spectrum can occur, then the number of bands observed in the experimental spectrum is not always equivalent to the number of vibrational modes predicted by group theory. The Raman spectra of the powders studied in this work obtained by the two preparation methods are shown in Figure 5.3.

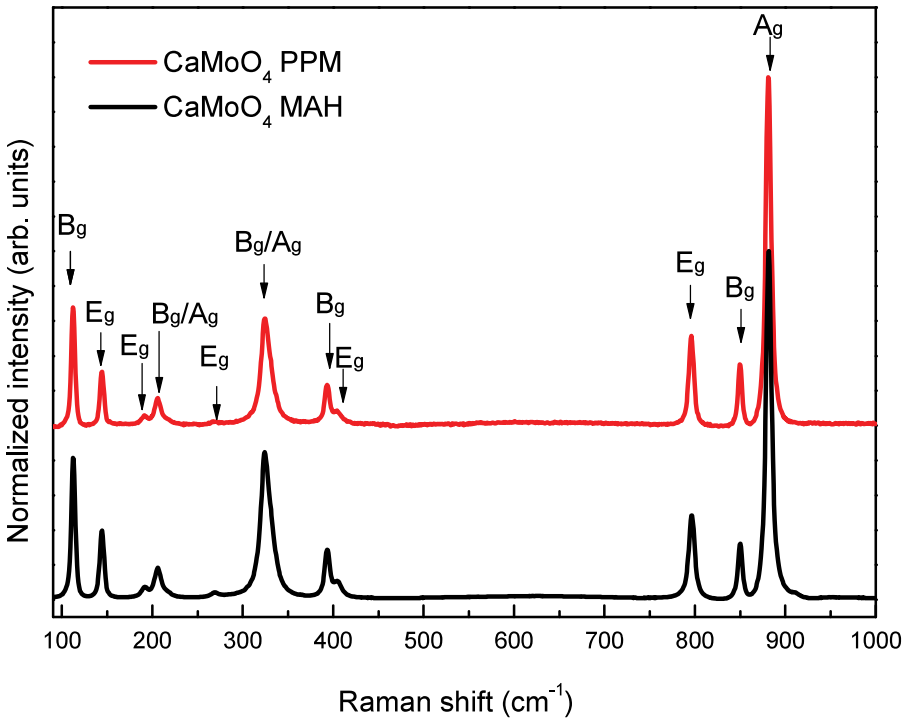

Figure 5.3. Raman spectra in the region of 50 to 1200 cm^{-1} for the $CaMoO_4$ powders prepared by MPP and HM.

Source: By the author.

The vibrational modes detected in the Raman spectrum for the molybdates can be classified into two groups, internal and external modes. External vibration modes are related to the phonon network or movement of $[CaO_8]$ clusters. Internal vibration modes are caused by the vibration of $[MoO_4]$ clusters, considering the center of mass at stationary state.[2,29-31] Therefore, micro-Raman spectra show that both methods produce $CaMoO_4$ without structural

alterations at medium-range despite the different morphologies which can be seen in the micrographs obtained by SEM (Fig. 5.2).

5.3.4 X-ray absorption spectroscopy measurements

X-ray absorption spectroscopy (XAS) measurements were performed on the $CaMoO_4$ PPM and $CaMoO_4$ MAH powders in order to investigate the short-range structural properties as well as their electronic structure. The Figure 5.4a shows the XANES spectra at Mo K-edge for $CaMoO_4$ PPM and $CaMoO_4$ MAH samples and MoO_3 standard reference. The pre-edge peaks in XANES spectra of $CaMoO_4$ samples are attributed to the transition from Mo 1s states to Mo 4d, which is dipole-allowed for tetrahedral symmetry because of the hybridization with O 2p states.[32] The same feature results in a shoulder for MoO_3 standard compound, which presents a distorted octahedral coordination.[33] As we have previously observed in $BaMoO_4$ samples,[34] no significant changes in these XANES spectra as a function of the preparation method were observed. It can assert that the first coordination shell around molybdenum atoms is formed by four oxygen atoms in a quite regular structure independently of the synthesis conditions.

Calculated XANES spectrum for $CaMoO_4$ compound using *ab initio* FEFF code[17] is also shown in Fig. 5.4b. The input files for FEFF code with cluster radius of 6.0 Å were initially generated using CRYSTALFFREV software[16] and crystallographic model according to XRD measurements. As can be seen in this Figure, calculated XANES spectra reproduce satisfactorily the experimental spectra. In order to elucidate the origin of the observed transitions, XANES spectra as a function of the cluster radius were calculated and shown in Fig. 5.4b with the illustration of each cluster. The theoretical spectra were calculated using clusters with radius equal to 1.77, 2.92, 3.69, 3.87, 4.08, 4.11, 4.14, 4.75, 5.23 and 6.0 Å. The

cluster with radius of 1.77 Å involves the first four O atoms around the absorbing Mo atom, whereas the cluster with radius equal to 2.92 Å involves the second (four atoms) shell of O atoms. In addition to these first eight neighbors, the cluster with radius equal to 3.69 Å encompasses the first four neighbors of Ca atoms, totaling 12 atoms around the Mo absorber atom. Four Ca atoms and four Mo atoms are inserted in the cluster with radius equal to 3.87 Å, totaling 20 atoms around the absorber atom. In addition to the atoms included in the cluster of radius equal to 3.87 Å, the clusters with radius equal to 4.08, 4.11, 4.14 and 4.75 Å consider, in this order, three shells with four O atoms and one shell with eight O atoms, resulting in a cluster of 40 atoms around the absorber Mo atom. In the cluster with radius of 5.23 Å is added a shell with four Mo atoms. Finally, the cluster with radius equal to 6.0 Å sums in the sequence the cluster of radius equal to 5.23 Å plus, in this order, three layers with four O atoms, one layer with two Ca atoms and one layer with three O atoms, a total of 62 atoms in the cluster.

As the cluster size is reduced between 4.08 and 4.14 Å, the oscillations are maintained with changes in intensity. In the spectra with cluster of radius less than 4.08 Å, the transitions labeled as B and C are not observed. As previously mentioned, the differences between clusters with radius of 4.08 and 4.14 Å are three shells of four O atoms each one. Thus, the shoulder in white line labeled as B and the transition labeled as C localized between 20020 and 20030 eV would have originated in these Mo-O interactions. The features labeled as E, G and H are observed up to the calculated spectrum with a cluster radius of 3.69 Å. This result indicates that these transitions are originated in the first four Mo-Ca interactions. The first four O neighbors of the absorbing Mo atom originate the transitions labeled as A, D and F, which can be observed in all spectra.

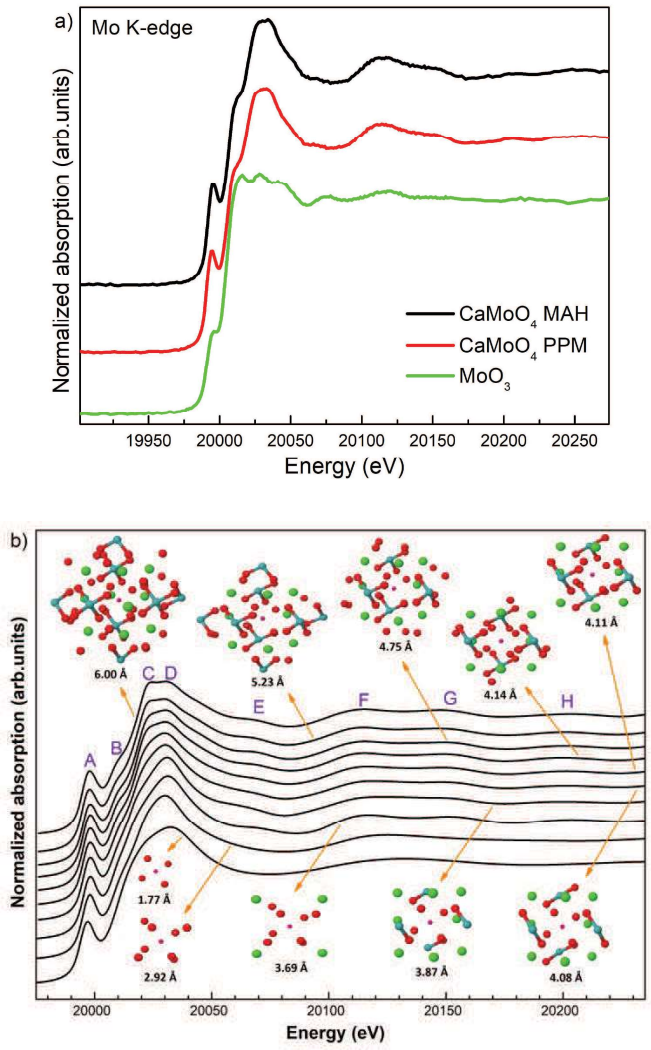

Figure 5.4 (a) XANES spectra at Mo K-edge of $CaMoO_4$ powders. (b) Theoretical XANES spectra as a function of cluster size. Pink, red, green and blue spheres represent Mo absorber atom, O, Ca and Mo atoms respectively.

Source: By the author.

The Figure 5.5 shows the modulus of k^3 weighted Fourier transform of $CaMoO_4$ samples extracted from Mo K-edge EXAFS spectra. According to the structural model calculated from the FEFF9 code and crystallographic information according the XRD measurements, the absorber atom is surrounded by, in this order, two shells with four O atoms each, two shells with four Ca atoms each, one shell with four Mo atoms and three shells with four O atoms each. Thus, the more intense peak, between 1.0 and 2.0 Å in the Fourier transforms, corresponds to a single scattering interaction between the first four O atoms

around the absorber atom. The single scattering interactions relative to Mo-Ca, Mo-Mo and Mo-O (beyond the first O neighbors) paths correspond the region observed between 2.0 and 5.0 Å. This region also includes multiple scattering.

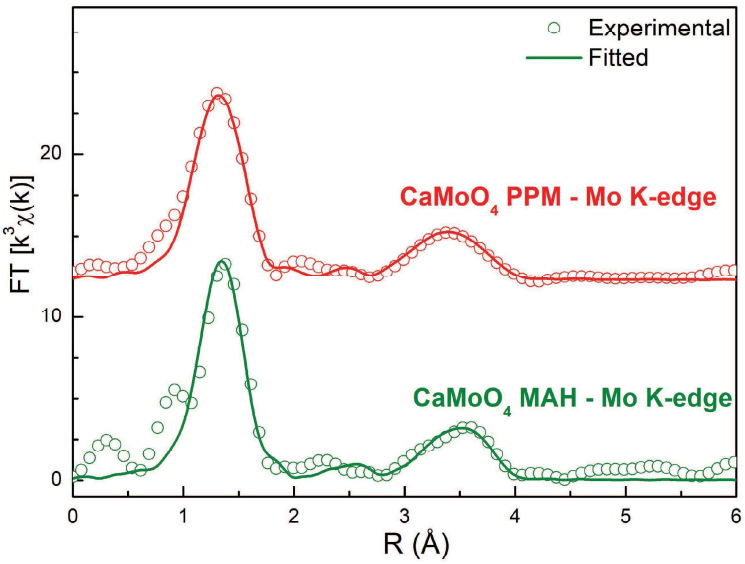

Figure 5.5. Experimental and fitted modulus of k^3 weighted Fourier transform for $CaMoO_4$ powders at Mo K-edge. Open symbols are experimental data, and solid lines represent fittings using the parameters listed in Table 5.1.
Source: By the author.

In order to obtain quantitative information of the local structure around Mo atoms, Fourier transform curves were then back Fourier transformed between 1.0 and 4.0 Å to obtain the experimental EXAFS spectra to fit using a theoretical model calculated from the FEFF9 code and crystallographic information according the XRD measurements. The results of the fits confirm that preparation method does not introduce high order disorders into the structure and do not change considerably the radial distance (R) for all shells. In all fits, the number of free parameters was kept smaller than the number of independent points, which is defined as $N_{ind} = 2\Delta R\Delta k/\pi$, where ΔR is the width of the R-space filter windows and ΔK is the actual interval of the fit in the k space.[33] The reliability of the fit, determined by a quality factor

(Q),[35] the interatomic distances (R) and Debye–Waller factor (σ^2) relatives to the best fits are shown in Table 5.1. As can be seen in this Table, no changes within the uncertainty are observed in the distance between each shell and Mo absorber atom comparing the two preparation methods. In the same way, Debye-Waller factor values do not exhibit alterations within the uncertainty. In other words, the preparation methods do not present effect on local structure, as well as without structural alterations at medium-range as shown in Raman analysis. This result reveals that MAH and PPM methods allow the fabrication of $CaMoO_4$ samples with different morphologies but without important lattice defects even though the completely different synthesis mechanisms and temperatures.

Table 5.1. Mo K-edge EXAFS simulation results. R is the distance from the central atom, N is the average coordination number, σ^2 the Debye–Waller factor, and Q the quality factor.

Shell	R (Å)		N		σ^2 (10^{-2} Å^2)		Q	
	MAH	PPM	MAH	PPM	MAH	PPM	MAH	PPM
Mo-O	1.76(1)	1.76(1)	4.1(2)	4.0(2)	0.19(8)	0.21(5)	4.39	1.76
Mo-O	2.91(4)	2.87(3)	2.4(6)	2.3(5)	1.2(2)	1.2 (1)		
Mo–Ca	3.72(2)	3.72(2)	3.3(1.1)	4.2(1.0)				
Mo–Ca	3.90(2)	3.88(1)	4.3(1.1)	4.6(0.8)				
Mo–Mo	4.2(2)	3.83(7)	4.7(6.9)	1.7(8.4)				
Mo–O	4.2(1)	4.0(7)	3.7(3.7)	5.8(3.0)				
Mo–O	4.02(1)	4.01(4)	4.0(1.5)	3.9(1.5)				
Mo-O	4.0(3)	3.9(2)	4.3(7.1)	4.2(7.1)				

Source: By the author.

5.4 Conclusions

Microwave-assisted hydrothermal and polymeric precursor methods were used to produce crystalline $CaMoO_4$ powders with a single scheelite-type tetragonal structure phase. SEM images reveal agglomerated rounded morphology in which particles present an average

diameter of nearly 100 nm and particles in clusters dumbbells-like shaped for PPM and MAH methods, respectively. Micro-Raman spectra show that both methods produce $CaMoO_4$ without important structural alterations, presenting only different morphologies. The XANES and EXAFS results of the fits confirm that preparation method does not introduce high order disorders into the structure.

ACKNOWLEDGMENTS

The authors gratefully acknowledge the financial support of the Brazilian research funding agencies FAPESP: 2013/07909-4 and 2013/07296-2, CAPES and CNPq: 470069/2013-9. The research was partially carried out at LNLS National Laboratory of Synchrotron Light (proposal number XAFS1−19058), Brazil.

5.5 References

1 KRÖGER, F. A. Luminescence of solid solutions of the system $CaMoO_4$ - $PbMoO_4$ and some others systems. **Philips Research Reports**, v. 2, p. 183-189, 1947.

2 VIEIRA, E. G. et al. Síntese pelo método da coprecipitação e caracterização estrutural do tungstato de cálcio com estrutura tipo scheelita. **Cerâmica**, v. 59, p. 417-425, 2013. doi:10.1590/S0366-69132013000300011.

3 ZHANG, Z. J. et al. Preparation and luminescent properties of $Eu^{3+}$and Tb^{3+}ions in the host of $CaMoO_4$. **Materials Science and Engineering B**, v. 145, p. 34-40, 2007. doi:10.1016/j.mseb.2007.09.091.

4 WANG, Y. G. et al. Low temperature synthesis of $CaMoO_4$ nanoparticles. **Ceramics International**, v. 33, p. 693-695, 2007. doi:10.1016/j.ceramint.2005.11.003.

5 MIKHAILIK, V. B. et al. Studies of electronic excitations in $MgMoO_4$, $CaMoO_4$ and $CdMoO_4$ crystals using VUV synchrotron radiation. **Physica Status Solidi B**, v. 242 , n. 2, p. 17-19, 2005. doi:10.1002/pssb.200409087.

6 YAO, W.; YE, J. Photophysical and photocatalytic properties of $Ca_{1-x}Bi_xV_xMo_{1-x}O_4$ solid solutions. **Journal of Physical Chemistry B**, v. 110, p. 11188 -11195, 2006. doi:10.1021/jp0608729.

7 CULVER, F. A. et al. Low-temperature synthesis of $AMoO_4$ (A = Ca, Sr, Ba) scheelite nanocrystals. Chemistry of Materials, v. 25, p. 4129−4134, 2013. doi:10.1021/cm402867y.

8 MARQUES, V. S. et al. Effect of different solvent ratios (water/ethylene glycol) on the growth process of $CaMoO_4$ Crystals and their optical properties. **Crystal Growth & Design**, v. 10, p. 4752-4768, 2010. doi:10.1021/cg100584b.

9 LONGO, V. M. et al. Hierarchical assembly of $CaMoO_4$ nano-octahedrons and their photoluminescence properties. **Journal of Physical Chemistry C**, v. 115, p. 5207-5219, 2011. doi:10.1021/jp1082328.

10 GHAED-AMINI, M; BAZARGANIPOUR, M.; SALAVATI-NIASARI, M. Calcium molybdate octahedral nanostructures, hierarchicalself-assemblies controllable synthesis by coprecipitation method: Characterization and optical properties. **Journal of Industrial and Engineering Chemistry**, v. 21, p 1089–1097, 2015. doi:10.1016/j.jiec.2014.05.019.

11 LUO, Y. S. et al. Controllable synthesis and luminescent properties of novel erythrocyte-like $CaMoO_4$ hierarchical nanostructures via a simple surfactant-free hydrothermal route. **Dalton Transactions**, v. 39, p. 2226-2231, 2010. doi:10.1039/b915099d.

12 SUN, Y. et al. Persimmon-like $CaMoO_4$ micro/nanomaterials: a rapid microwave-assisted fabrication, characterization, and the growth mechanism. **Solid State Sciences**, v. 14, p .219-224, 2012. doi:10.1016/j.solidstatesciences.2011.11.015.

13 YOON, J. W.; RYU, J. H.; SHIM, K. B. Photoluminescence in nanocrystalline $MMoO_4$ (M = Ca, Ba) synthesized by a polymerized complex method. **Materials Science and Engineering B**, v. 127, p. 154–158, 2006. doi:10.1016/j.mseb.2005.10.015.

14 MARQUES, A. P. A. et al. Evolution of photoluminescence as a function of the structural order or disorder in $CaMoO_4$ nanopowders. **Journal of Applied Physics**, v. 104, p. 043505 (6), 2008. doi:10.1063/1.2968388.

15 MESQUITA, A.; MICHALOWICZ, A.; MASTELARO, V. M. XANES measurements probing the local order and eletronic structure of $Pb_{1-x}Ba_xZr_{0.40}Ti_{0.60}O_3$ ferroeletric materials. **Journal of Alloys and Compounds**, v. 640, p. 355-361, 2015. doi:10.1016/j.jallcom.2015.04.015.

16 MICHALOWICZ, A. et al. MAX: Multiplatform applications for XAFS. **Journal of Physics: Conference Series**, v. 190, p. 012034 (4), 2009. doi:10.1088/1742-6596/190/1/012034.

17 ANKUDINOV, A. L. et al. Real-space multiple-scattering calculation and interpretation of x-ray-absorption near-edge structure. **Physical Review B**, v. 58, n. 12, p. 7565-7576, 1998. doi:10.1103/PhysRevB.58.7565.

18 CULLITY, D. B., **Elements of X-ray Diffraction**, Addison-Wesley Inc., Massachusetts; 1956.

19 THONGTEM, T.; PHURUANGRAT, A; THONGTEM, S. Synthesis of $CaWO_4$, $SrWO_4$ and $BaWO_4$ with nanosized particles using cyclic microwave radiation. **Journal of Ceramic Processing Research**, v. 9, n. 3, p. 258-261, 2008.

20 WANG, G.; LIN, S.; WAN, G. Growth process and optical properties of $SrWO_4$ microcrystal prepared by a microwave-assisted method. **Synthesis and Reactivity in Inorganic, Metal-Organic, and Nano-Metal Chemistry**, v. 42, p. 888-891, 2012. doi:10.1080/15533174.2011.652283.

21 ZHANG, L. et al. Dumbbell-like $BaWO_4$ microstructures: surfactant-free hydrothermal synthesis, growth mechanism and photoluminescence property. **Superlattices and Microstructures**, v. 54, p. 87-95, 2013. doi:10.1016/j.spmi.2012.11.010.

22 LU, Y. et al. Large-scale controllable synthesis of dumbbell-like $BiVO_4$ photocatalysts with enhance visible-light photocatalytic activity. **Journal of Solid State Chemistry**, v. 186, p. 255-260, 2012. doi:10.1016/j.jssc.2011.12.003.

23 CHEN, Z. et al. Controllable synthesis of Hierarchical nanostructures of $CaWO_4$ and $SrWO_4$ via facile low-temperature route. **Materials Research Bulletin**, v. 44, p. 45-50, 2009. doi:10.1016/j.materresbull.2008.04.008.

24 LI, Y. F. at al. Room-temperature template-free synthesis of dumbbell-like $SrSO_4$ with hierarchical architecture. **Journal of Crystal Growth**, v. 312, p. 1886-1890, 2010. doi:10.1016/j.jcrysgro.2010.03.007.

25 JAYARAMAN, A.; BATLOGG, B.; VANUITERT, L. G. High-pressure Raman study of alkaline-earth tungstates and a new pressure-induced phase transition in $BaWO_4$. **Physical Review B**, v. 28, p. 4774-4777, 1983. doi:10.1103/PhysRevB.28.4774.

26 JAYARAMAN, A.; WANG S. Y.; SHARMA, S. K. High-pressure Raman investigation on $CdMoO_4$ and pressure-induced phase transformations. **Physical Review B**, v. 52, p. 9886-9889, 1995. doi:10.1103/PhysRevB.52.9886.

27 PORTO, S. P. S.; SCOTT, J. F. Raman spectra of $CaWO_4$, $SrWO_4$, $CaMoO_4$, and $SrMoO_4$. **Physical Review**, v. 157, p. 716-719, 1967. doi:10.1103/PhysRev.157.716.

28 MANJÓN, F. J et al. Lattice dynamics study of scheelite tungstates under high pressure I. $BaWO_4$. **Physical Review B**, v. 74, p. 144111 (17), 2006. doi:10.1103/PhysRevB.74.144111.

29 CAVALCANTE, L. S. et al. Synthesis, characterization, anisotropic growth and photoluminescence of $BaWO_4$. **Crystal Growth and Design**, v. 09, p. 1002-1012, 2009. doi:10.1021/cg800817x.

30 SCZANCOSKI, J. C. et al. Electronic structure and optical properties of $BaMoO_4$ powders. **Current Applied Physics**, v. 10, p. 614-624, 2010. doi:10.1016/j.cap.2009.08.006.

31 CAVALCANTE, L. S. et al. $BaMoO_4$ powders processed in domestic microwave-hydrothermal: synthesis, characterization and photoluminescence at room temperature. **Journal of Physics and Chemistry of Solids**, v. 69, p. 2674-2680, 2008. doi:10.1016/j.jpcs.2008.06.107.

32 GRACIA, L. et al. Presence of excited electronic state in $CaWO_4$ crystals provoked by tetrahedral distortion: An experimental and theoretical investigation. **Journal of Applied Physics**, v. 110, p. 043501 (11), 2011. doi:10.1063/1.3615948.

33 ROCCA, F. et al. XANES and EXAFS at Mo K-edge in $(AgI)_{1-x}(AgMoO_4)_x$ glasses and crystals. **Solid State Ionics**, v. 121, p. 189-192, 1999.

34 ALENCAR, L. D. S. et al. Preparation, characterization and catalytic application of Barium molybdate ($BaMoO_4$) and Barium tungstate ($BaWO_4$) in the gas-phase oxidation of toluene. **Ceramics International**, v. 43, n. 5, p. 4462–4469, 2017. doi:10.1016/j.ceramint.2016.12.096.

35 HASNAIN, S. S. Report on the International Workshops on Standards and Criteria in XAFS. **X-ray Absorption Fine Structure**: Proceedings of the VI International Conference on X-ray Absorption Fine Structures, Ellis Horwood, New York, 1991.

6 CONCLUSIONS

Microwave-assisted hydrothermal and polymeric precursor methods produced crystalline $BaWO_4$, $BaMoO_4$, $CaWO_4$ and $CaMoO_4$ powders with scheelite-type tetragonal structure with space group $I4_1/a$ without diffraction peaks related to secondary phase. SEM-FEG micrographs showed that all powders prepared by the polymeric precursors method present rounded shape with agglomerated nature while $BaWO_4$ and $BaMoO_4$ powders prepared by microwave-assisted hydrothermal method present shuttle-like crystals with four prominences in the middle part, with polydisperse particles sizes distribution and $CaWO_4$ and $CaMoO_4$ powders synthesized by microwave-assisted hydrothermal method have dumbbell-like morphology due polymeric agents and processing using microwave. The XANES and EXAFS results of the fits confirm that preparation method does not introduce high order disorders into the structure. From the EXAFS results we could state that the oxygen vacancies are introduced in $BaWO_4$ and $BaMoO_4$ samples and apparently the $BaWO_4$ samples present increased the content of oxygen vacancies relative to the $BaMoO_4$ samples. $BaWO_4$, $BaMoO_4$ and $CaWO_4$ powders were employed as solid catalysts towards gas phase toluene oxidation reactions and $BaWO_4$ by MAH showed higher catalytic activity at 400 ºC. The H_2-TPR results indicated that $BaWO_4$ samples, compared with $BaMoO_4$ samples, have higher oxygen mobility that appear as key factors for the achievement of better catalytic performances. The same result was found for $CaWO_4$ sample prepared by MAH compared with $CaWO_4$ sample prepared by PPM. PL emissions at room temperature of $BaWO_4$, $BaMoO_4$ and $CaWO_4$ powders were attributed to the charge-transfer transitions within the $[WO_4]^{2-}$ and $[MoO_4]^{2-}$ complexes.

APPENDIX

A. Additional characterizations

A.1 Optical characterizations of $CaMoO_4$

$CaMoO_4$ powders were characterized by photoluminescence spectroscopy and UV/Vis absorption spectroscopy. The characterization methods and equipment used were the same as those reported in *Papers 1* and *2*.

A.1.1 Photoluminescence

The emission spectra of $CaMoO_4$ powders are shown in Figure A.1. These materials also have photoluminescence when excited at 350 nm, with emisson peaks at 513 nm and 511 nm to $CaMoO_4$ synthesized by PPM and HAM, respectively.

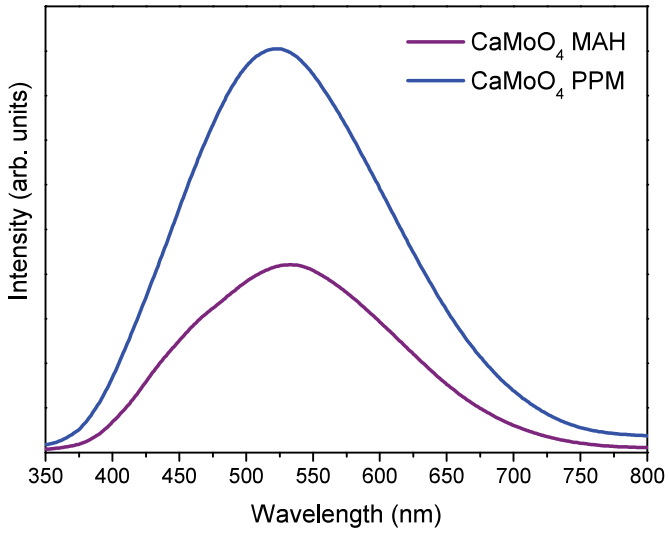

Figure A.1. PL spectra of $CaMoO_4$ powders (λ_{EXC} = 350 nm). The maximum emission peaks are centered on 513 nm and 511 nm for PPM and MAH, respectively.
Source: By the author

For both $CaMoO_4$ and others molybdates, we understand that this luminescence is associated with the disorder caused by $[MoO_4]^{2-}$ and to the charge-transfer transitions within the $[MoO_4]^{2-}$ complexes.[1,2]

A.1.2 UV/Vis absorption spectroscopy

The Figure A.2 presents the UV/Visible spectroscopy of $CaMoO_4$ powders performed in the diffuse reflectance mode and the optical band gap (E_{gap}) estimated by method proposed by Kubelka and Munk.[3,4]

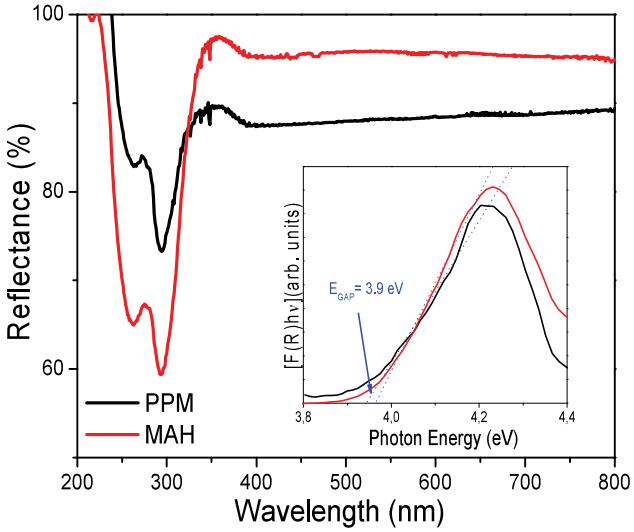

Figure A.2. UV/Vis spectra of $CaMoO_4$ powders processed in MAH and PPM. The inset shows the obtained optical band gap.
Source: By the author

The *Egap* value found for CaMoO4 materials, which was 3.9 eV for both PPM and MAH, are in agreement with other values reported in the literature.[5,6]

A.2 Micro-Raman spectroscopy of $BaWO_4$, $BaMoO_4$ and $CaWO_4$ powders

Raman spectroscopy is a technique that consists of the inelastic scattering of visible light by molecules. As a result of this physical phenomenon, there is a change between the frequencies of scattered and incident light that allows the identification of molecular structures by their vibrational modes. Micro-Raman spectra of $BaWO_4$, $BaMoO_4$ and $CaWO_4$ powders were obtained as described in *Paper 3*.

The Raman spectra are shown in Figure A.3. The vibrations of $CaWO_4$, $BaWO_4$ and $BaMoO_4$ materials are the same as those reported for $CaMoO_4$, reported in *Paper 3*.[7-10]

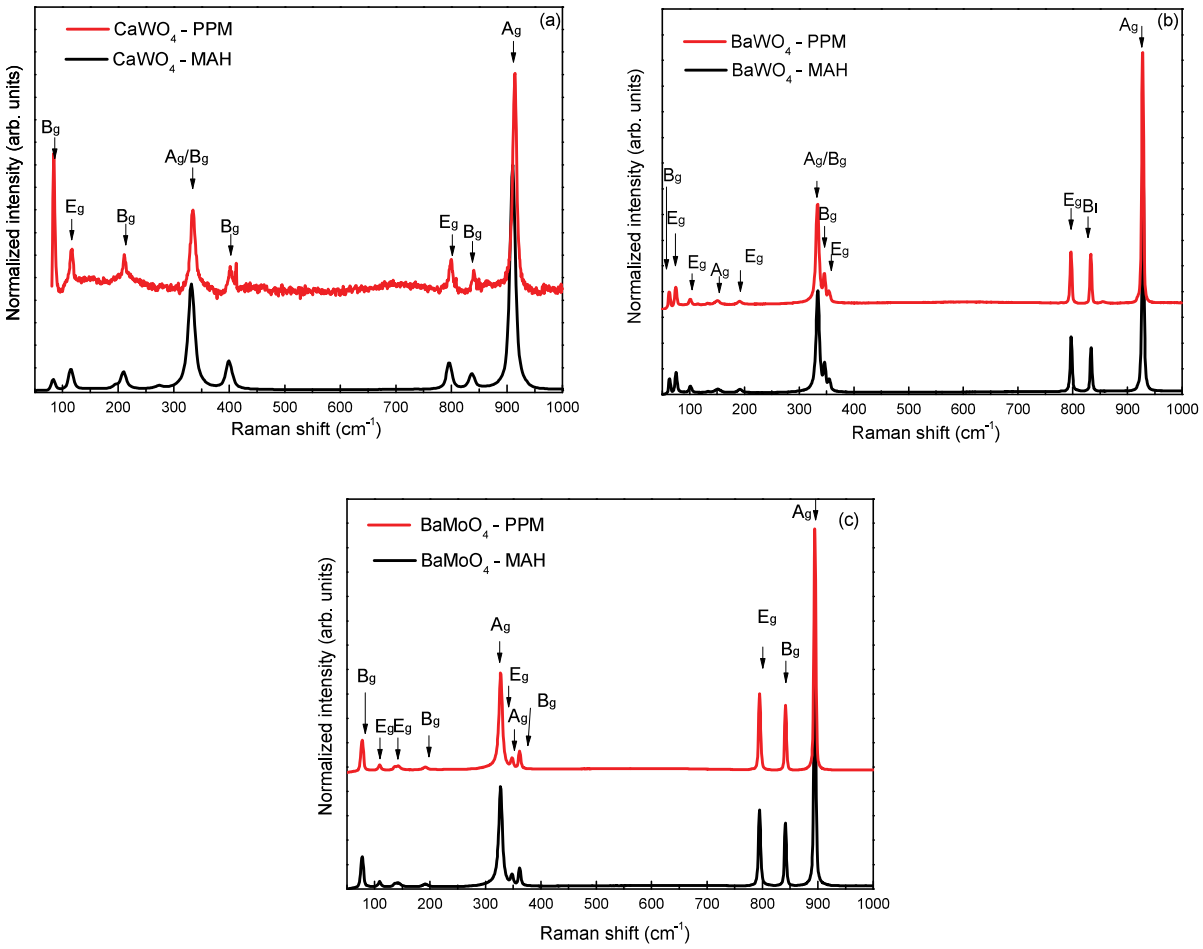

Figure A.3. Raman spectra in the region of 50 to 1000 cm^{-1} for (a) $CaWO_4$, (b) $BaWO_4$ and (c) $BaMoO_4$ powders prepared by MPP and HM.

Source: By the author

The vibrational modes detected in the Raman spectrum for the molybdates and tungstates can be classified into two groups, internal and external modes. External vibration modes are related to the phonon network or movement of $[CaO_8]$ and $[BaO_8]$ clusters. Internal vibration modes are caused by the vibration of $[MoO_4]$ and $[WO_4]$ clusters, considering the center of mass at stationary state.[2,4,11-12]

A.3 References

1 SCZANCOSKI, J. C. et al. Electronic structure and optical properties of $BaMoO_4$ powders. **Current Applied Physics**, v. 10, p. 614-624, 2010. doi:10.1016/j.cap.2009.08.006.

2 CAVALCANTE, L. S. et al. $BaMoO_4$ powders processed in domestic

microwave-hydrothermal: synthesis, characterization and photoluminescence at room temperature. **Journal of Physics and Chemistry of Solids**, v. 69, p. 2674-2680, 2008. doi:10.1016/j.jpcs.2008.06.107.

3 KUBELKA, P.; MUNK, F. Ein Beitrag Zur Optik Der Farbanstriche. **Zeitschrift für Technische Physik**, v. 12, p. 593-603, 1931.

4 SCZANCOSKI, J. C. et al. Electronic structure and optical properties of $BaMoO_4$ powders. **Current Applied Physics**, v. 10, p. 614-624, 2010. doi:10.1016/j.cap.2009.08.006.

5 LONGO, V. M. et al. Hierarchical assembly of $CaMoO_4$ nano-octahedrons and their photoluminescence properties. **Journal of Physical Chemistry C**, v. 115, p. 5207-5219, 2011. doi:10.1021/jp1082328.

6 LONGO, V. M. et al. Different origins of green-light photoluminescence emission in structurally ordered and disordered powders of calcium molybdate. **Journal of Physical Chemistry A**, v. 112, p. 8920-8928, 2008. doi:10.1021/jp801587w.

7 JAYARAMAN, A.; BATLOGG, B.; VANUITERT, L. G. High-pressure Raman study of alkaline-earth tungstates and a new pressure-induced phase transition in $BaWO_4$. **Physical Review B**, v. 28, p. 4774-4777, 1983. doi:10.1103/PhysRevB.28.4774.

8 JAYARAMAN, A.; WANG S. Y.; SHARMA, S. K. High-pressure Raman investigation on $CdMoO_4$ and pressure-induced phase transformations. **Physical Review B**, v. 52, p. 9886-9889, 1995. doi:10.1103/PhysRevB.52.9886.

9 PORTO, S. P. S.; SCOTT, J. F. Raman spectra of $CaWO_4$, $SrWO_4$, $CaMoO_4$, and $SrMoO_4$. **Physical Review**, v. 157, p. 716-719, 1967. doi:10.1103/PhysRev.157.716.

10 MANJÓN, F. J et al. Lattice dynamics study of scheelite tungstates under high pressure I. $BaWO_4$. **Physical Review B**, v. 74, p. 144111 (17), 2006. doi:10.1103/PhysRevB.74.144111.

11 VIEIRA, E. G. et al. Síntese pelo método da coprecipitação e caracterização estrutural do tungstato de cálcio com estrutura tipo scheelita. **Cerâmica**, v. 59, p. 417-425, 2013. doi:10.1590/S0366-69132013000300011.

12 CAVALCANTE, L. S. et al. Synthesis, characterization, anisotropic growth and photoluminescence of $BaWO_4$. **Crystal Growth and Design**, v. 09, p. 1002-1012, 2009. doi:10.1021/cg800817x.

ATTACHMENT

I.Permission granted to use published manuscript: Paper 1

What rights do I retain as an author?

Last updated on 09/02/2017 11.46 AM

As an author, you retain rights for a large number of author uses, including use by your employing institute or company. These rights are retained and permitted without the need to obtain specific permission from Elsevier. These include:

- The right to include the article in full or in part in a thesis or dissertation (provided that this is not to be published commercially).

Available at: <https://service.elsevier.com/app/answers/detail/a_id/565/>. Accessed: March 19, 2018.

II. Permission granted to use published manuscript: Paper 2

Luciana <vlrz@ufscar.br> Mar 20

to me

Dear Lorena Alencar

Permission granted to use the manuscript entitled "Effect of different synthesis methods on the textural properties of calcium tungstate ($CaWO_4$) and its catalytic properties in the toluene oxidation" in your thesis.

Best regards,
Luciana Zanotto
Materials Research
Editorial Assistant

III. Confirmation of submission: Paper 3

Thank you for your submission to Materials Science and Engineering B Inbox x

Materials Science & Engineering B <eesserver@eesmail.elsevier.com> Mar 6 (4 days ago)

to me

Dear Mrs. Alencar,

Thank you for sending your manuscript Short- and long-range structural characterization of $CaMoO_4$ powders prepared by microwave assisted hydrothermal and polymeric precursor methods for consideration to Materials Science and Engineering B. Please accept this message as confirmation of your submission.